PLOS COMPUTATIONAL BIOLOGY

RESEARCH ARTICLE

Spatial distribution of cytoskeleton-mediated feedback controls cell polarization: A computational study

Parijat Banerjee[1], Jonathan A. Kuhn[2], Dhiman Sankar Pal[2¤], Yu Deng[2], Tatsat Banerjee[2], Peter N. Devreotes[2], Pablo A. Iglesias[2,3*]

1 Department of Physics and Astronomy, Johns Hopkins University, Baltimore, Maryland, United States of America, **2** Department of Cell Biology and Center for Cell Dynamics, School of Medicine, Johns Hopkins University, Baltimore, Maryland, United States of America, **3** Department of Electrical and Computer Engineering, Johns Hopkins University, Baltimore, Maryland, United States of America

¤ Current address: Department of Biological Sciences, Hunter College, The City University of New York, New York, New York, United States of America
* pi@jhu.edu

OPEN ACCESS

Citation: Banerjee P, Kuhn JA, Pal DS, Deng Y, Banerjee T, Devreotes PN, et al. (2025) Spatial distribution of cytoskeleton-mediated feedback controls cell polarization: A computational study. PLoS Comput Biol 21(10): e1013036. https://doi.org/10.1371/journal.pcbi.1013036

Editor: Calina Copos, Northeastern University, UNITED STATES OF AMERICA

Received: April 10, 2025

Accepted: September 25, 2025

Published: October 9, 2025

Data availability statement: Data and code are available on Zenodo: doi: 10.5281/zenodo.15178618.

Funding: National Institute of General Medical Sciences of the National Institutes of Health under award numbers R01GM149073 (to P.A.I.) and R35GM118177 (to P.N.D.) https://www.nigms.nih.gov. The funders did not play any role in the study design, data collection and analysis, decision to publish, or preparation of the manuscript.

Abstract

In the social amoeba *Dictyostelium*, cell motility is regulated through a signal transduction excitable network that interfaces with the cytoskeleton to control actin polymerization patterns. In turn, the cytoskeleton influences the signaling machinery via several feedback loops, but the nature and function of this feedback remain poorly understood. In this study, we use computational models to discern the essential role of complementary positive and negative feedback loops in polarizing cells. We contrast two potential mechanisms for the negative feedback: local inhibition and global inhibition. Our results indicate that both mechanisms can stabilize the leading edge and inhibit actin polymerization in other sites, preventing multipolarity. While some experimental perturbations align more closely with the local inhibition model, statistical analyses reveal its limited polarization potential within a wide excitability range. Conversely, global inhibition more effectively suppresses secondary and tertiary leading-edge formation, making it a more robust polarization mechanism. This raises an intriguing question: if local inhibition better replicates experimental observations but is less effective for polarization than local excitation and global inhibition, could there be a supplementary mechanism enhancing its polarization potential? To address this, we propose a novel mechanism involving the dynamic partitioning of back molecules which enhances communication between the front and back of the cell and can be leveraged by local feedback interactions between the cytoskeleton and signal transduction to improve polarization efficiency.

Author summary

Cells use a network of signaling molecules to move and organize themselves, creating distinct front and back regions. Although we know that the cell's structure influences

Competing interests: The authors have declared that no competing interests exist.

these signals, the details of how they work together are not fully understood. In this study, we used computational models to study how feedback mechanisms help cells maintain this polarity. We first looked at two types of negative feedback: local feedback, where signals inhibit activity near the site of activity, and global feedback, where inhibition spreads throughout the entire cell. Our simulations showed that both types can stabilize the front of the cell and prevent it from developing multiple leading edges. However, while local feedback closely matched experimental results, it was less effective in maintaining direction under varying conditions. Global feedback proved to be more reliable in preventing the formation of additional leading edges. To address this, we introduced a new idea involving the release and diffusion of molecules, which enhances feedback and improves how well the cell can maintain its direction. Understanding how cells polarize in this way has important implications, such as improving our knowledge of development processes and disease progression.

Introduction

Directed cell motility, the ability of motile cells to sense external cues and use these to navigate, is a fundamental process in various biological contexts, including embryonic development, wound healing, and immune responses. To migrate, cells must develop a spatial asymmetry consisting of well-defined front and rear components. Proteins that localize to either region can be described as front or back markers. The former includes signaling proteins such as Ras and PI3K that regulate actin polymerization, as well as cortical proteins that give rise to protrusions, including actin and actin-binding proteins such as cofilin, coronin, or Arp2/3. Similarly, the rear is marked by various signaling markers (e.g. $PI(4,5)P_2$, PTEN, PIP5K), as well as cortical proteins such as myosin II and cortexillin that provide contractility.

Cell polarity can arise in response to spatially heterogeneous chemical or mechanical cues from the environment. These external signals induce internal asymmetries that are temporal — once the cue is removed, the cell reverts to its pre-stimulus, unpolarized state. For example, Latrunculin-treated *Dictyostelium* cells, which have inhibited actin polymerization, form crescents of intracellular markers aligned with a chemoattractant gradient despite their impaired motility [1,2]. However, when the chemoattractant is removed, these cells lose their asymmetry and reorient homogeneously. Alternatively, symmetry breaking can result in a polarized state that persists even after the stimulus is withdrawn; for instance, *Dictyostelium* cells moving toward a gradient maintain their directionality after the cue is removed [3]. To distinguish between these processes, we refer to stable spatial asymmetries as *polarization*, while transient responses to spatially heterogeneous stimuli are described as gradient sensing [3]. Here, we focus primarily on polarization. Note that cells can also spontaneously polarize from stochastic spatial heterogeneities that become amplified and stabilized.

In parallel to the polarization process, cell motility involves dynamic spatial patterning driven by the interaction of two excitable systems: the signal transduction excitable network (STEN) and the cytoskeleton excitable network (CEN). Although these systems are coupled, both exhibit excitability independently when the other is eliminated [4]. It is well-established that the signaling patterns generated by STEN coordinate the actions of CEN to drive migration. There is also substantial evidence that feedback from CEN also influences STEN [5]. While actin polymerization provides positive feedback to signaling at the front of the cell [2,6–17], at the rear, myosin is involved in distinct feedback loops [18–20]. Ras/PI3K activation promotes myosin disassembly [21–23], and recent findings in *Dictyostelium* show that myosin assembly inhibits Ras/PI3K activation [24]. These findings suggest the presence of a

double negative feedback loop — functionally equivalent to positive feedback — that operates at the rear of migrating cells.

In this paper, we explore the interaction between these two patterning phenomena to understand how feedbacks arising from coupled excitable systems can stabilize to form polarized cells (Fig 1). To achieve this, we rely on computational modeling. The study of spatial patterns has long benefited from mathematical models, beginning with Alan Turing's pioneering concept of morphogenesis—the development of spatial patterns from an initially homogeneous state [25]. Turing's work showed how differential diffusion properties between activating and inhibiting processes could destabilize homogeneous states, leading to the emergence of patterns. Building on this, Meinhardt and Gierer formalized a model based on local self-enhancing activation and lateral inhibition (LALI) [26]. The minimal LALI model proposes two interacting species: a local activator with low diffusivity and strong autocatalytic properties that amplifies initial asymmetries and a lateral inhibitor, and a more diffusible antagonist that provides negative feedback to confine the pattern to specific regions. This general framework is ubiquitous in biological systems. Canonical examples of excitability also take the form of activator-inhibitor systems [27,28] where a single equilibrium is stable. Numerous models have been developed to describe the cytoskeletal dynamics [29–31] and signaling behavior in migrating cells [32–37]. Some of these models address the coupled interaction between signaling and the cytoskeleton [38–41], while others focus on how these excitable patterns drive cell movement [38,42–52]. Previous models have shown that the combination of local positive and global negative feedback can polarize cells [38,45]. Experiments have suggested that global inhibition could be effected through increased cortical/membrane tension [53–55]. Recent findings in *Dictyostelium* cells suggest the presence of a local inhibitory feedback loop mediated by actomyosin at the rear of the cell [24,56]. Recent experiments have also revealed that active Ras, a key component of STEN, regulates PIP5K binding to the membrane. This

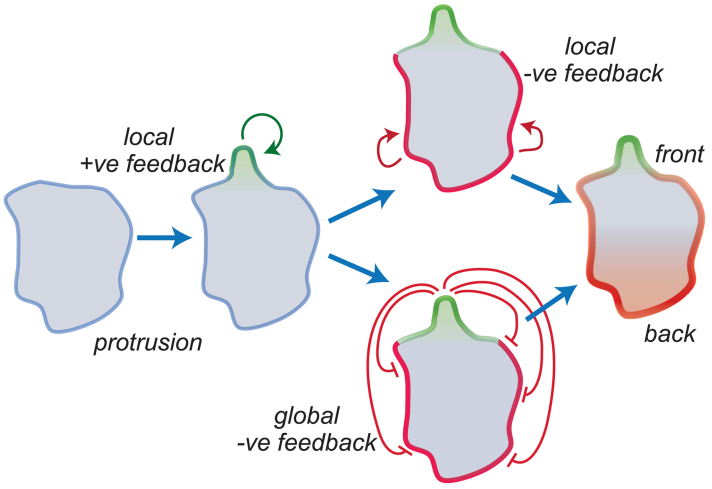

Fig 1. Cytoskeletal-mediated feedback loops influence STEN activity. Regions of elevated Ras lead to localized actin polymerization, initiating a positive feedback loop that further increases Ras production and leads to a nascent protrusion (left). In this paper we consider two putative negative feedback loops. In the first (middle top), the Ras inhibitors at the rear of the cell prevent the formation of protrusions away from the initial one. In the second (middle bottom), the appearance of the protrusion propagates inhibition to the rear; for example, through increased cortical or membrane tension. The interplay between these feedback loops contributes to the stabilization of the front-rear axis in cells (right).

https://doi.org/10.1371/journal.pcbi.1013036.g001

suggests a means by which a single molecule may provide both local positive feedback as well as the lateral, or global, inhibition. Through simulation, we show how this mechanism can help to polarize cells. Our aim is to understand the relative roles of positive and negative feedback loops from the cytoskeleton to the signaling network and how their spatial distribution defines stable patterns within the excitable system.

Results

The core excitable system

To explore cell patterning in the absence of an intact cytoskeleton, we revisited a computational model of the signal transduction system in *Dictyostelium* (Methods). This model (Fig 2A) consists of three interacting species — Ras, $PI(4,5)P_2$, and PKB — that form the core of an excitable network. Ras and $PI(4,5)P_2$ exhibit mutually inhibitory interactions, partitioning the membrane into complementary domains: regions of high Ras activity correspond to low $PI(4,5)P_2$ levels, and vice versa [57]. This double-negative feedback loop generates the classical positive feedback essential for excitability. PKB serves as the network's refractory component, activated by Ras but providing slow, negative feedback to suppress Ras activity [16,58]. The model was implemented using coupled stochastic reaction-diffusion equations in both one- and two-dimensional environments (Methods).

Simulations of this model in a one-dimensional periodic domain exhibited occasional firings characteristic of excitable systems. Following these firings, distinct traveling waves emerged from the site of excitation, propagating laterally in both directions and forming V-shaped patterns in kymographs, where the tip of the "V" indicates the initiation point of the wave (Fig 2B). The stochastic nature of the model resulted in spatial asymmetries, causing one arm of the "V" to extinguish before the other. As depicted in the kymograph, $PI(4,5)P_2$ and Ras levels were complementary, with PKB exhibiting patterns similar to those of Ras but with a slower decay. The durations of Ras and PKB firings were 51.6 ± 48.4 s and 96.9 ± 39.8 s, respectively (Fig 2C; mean $\pm$ s.d.; $n = 159$ firings).

In the model, the initiation of a firing is a purely stochastic event, where molecular noise drives the system sufficiently far from the unique dynamic stable equilibrium, resulting in a stereotypical all-or-nothing response typical of excitable systems. To quantify the duration of this response, we measured the temporal autocorrelation of Ras activity at each spatial point in the kymograph (Fig 2D). This analysis revealed a small correlation, which dropped to 0.1 within approximately 60 s (Fig 2D). At longer time scales, there was little memory of the initial excitation.

To compare with experimental data, we imaged Latrunculin-treated *Dictyostelium* cells and created kymographs of Ras-GFP around the perimeter (Fig 2E–2G). These cells also displayed spontaneous patches of activity around the perimeter, with sizes of approximately 50° and durations of about 60 s.

Morphological differences drive cell motility efficiency

To examine the correlation between cell shape (polarity) and cell movement, we imaged unstimulated *Dictyostelium* cells and quantified their circularity. We identified three broad classifications: cells exhibiting long, narrow shapes (circularity values less than 0.25; Fig 3A and S1 Video), cells with little eccentricity (circularity values greater than 0.45; Fig 3C and S3 Video) and an intermediate group of cells, occasionally displaying some polarized morphology, with circularity values between these 0.25 and 0.45; Fig 3B and S2 Video). To correlate these cellular morphologies with cell movement, we computed the total distance traveled,

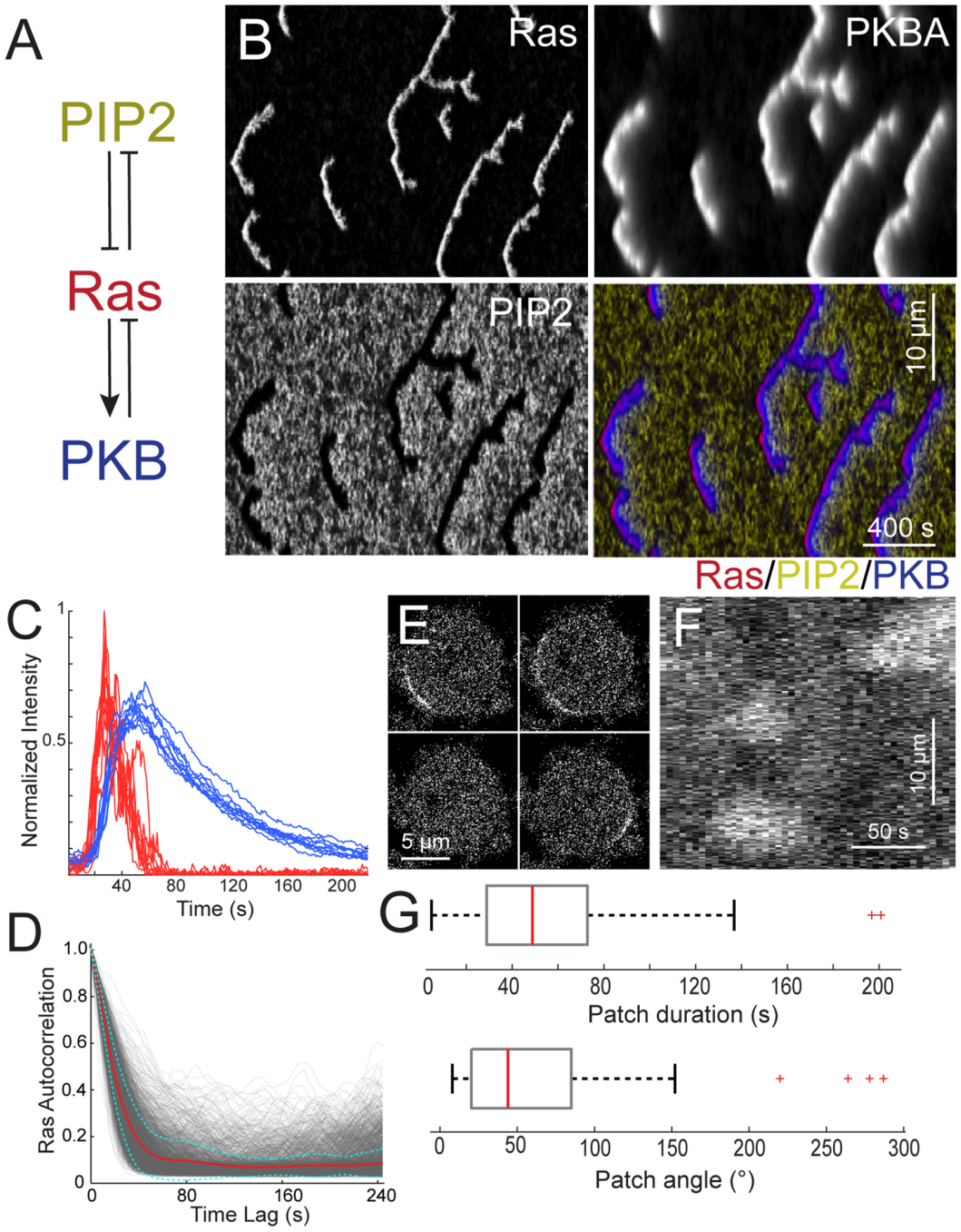

Fig 2. Cells lacking a cytoskeleton display patches with low temporal correlation. A. Schematic of the STEN model incorporating Ras, PIP2 and PKB (Methods). B. Representative kymographs of each of STEN components showing spatial and temporal behavior for an unstimulated cell. C. Traces of 16 simulated firings, showing Ras (red) and PKB (blue). D. Ras temporal correlation from simulations (4 simulations; 126 traces each). The red line shows the average of all the traces; the cyan lines are mean ± std. E. Images of a Latrunculin-treated *Dictyostelium* cell displaying RBD-GFP. F. Corresponding kymograph around the perimeter. G. Box plot for the patch duration and angular size for the RBD-GFP patches ($n = 81$ patches in 15 cells).

https://doi.org/10.1371/journal.pcbi.1013036.g002

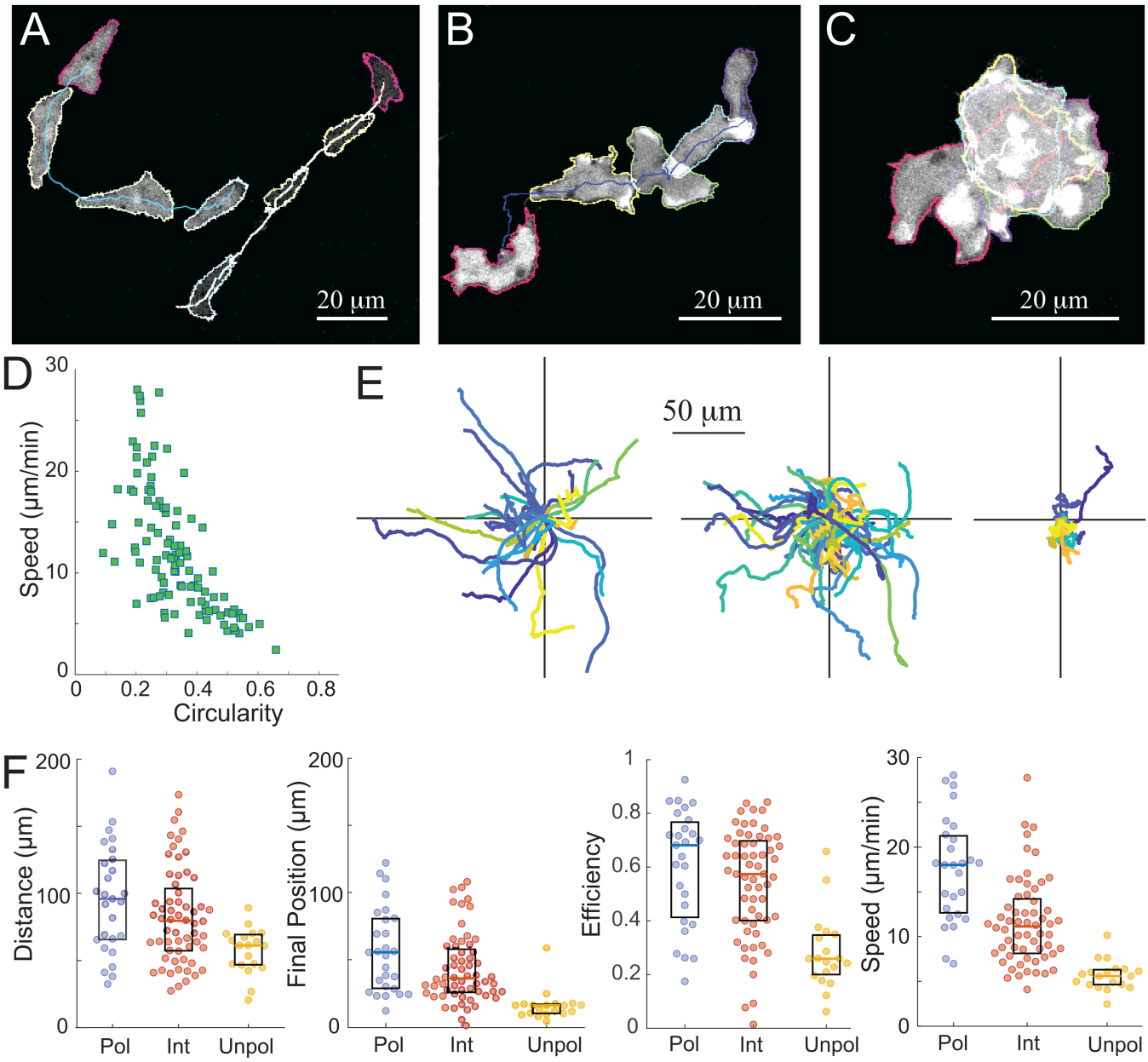

Fig 3. Correlation between shape and movement. A-C. *Dictyostelium* cells were imaged over time, and their shape and displacement were measured over time. Cells displayed polarized (A; S1 Video), intermediate (B; S2 Video) or unpolarized morphologies (C; S3 Video). The snapshots here show cells 120 seconds apart. D. Correlation between speed (centroid) and circularity. E. Displacement over time for cells in the three classes. These were chosen based on the average circularity over time. Polarized cells have circularity less the 0.25; intermediate cells have circularity between 0.25 and 0.45; and unpolarized cells have circularities greater than this. F. Total distance, final position, efficiency (final position/total distance) and centroid speed for the various cells in the three classes. Total number of cells were 27, 60 and 19, respectively.

https://doi.org/10.1371/journal.pcbi.1013036.g003

final position, efficiency (the ratio of the previous two values), and centroid speed of the cells and found the correlation with circularity (Fig 3D). The corresponding Pearson correlations were $\rho = -0.34$, $p < 3 \times 10^{-4}$ (total distance traveled), $\rho = -0.48$, $p < 2 \times 10^{-7}$ (final position), $\rho = -0.51$, $p < 2 \times 10^{-8}$ (efficiency) and $\rho = -0.67$, $p < 3 \times 10^{-15}$ (speed) from $n = 106$ cells. Polarized cells moved in relatively straight lines (Fig 3E) and traveled the farthest distances

(Fig 3F). When these cells turned, they did so in gradual arcs. At the opposite extreme, cells with little eccentricity despite being active and displaying deviations from a circular shape, did not maintain a consistent form. In this case, the centroid did not exhibit significant movement. Finally, cells in the intermediate group moved a moderate distance, but they often came to a stop. Occasionally, they would adopt a shape perpendicular to their previous movement. We also plotted kymographs of Ras activity around the perimeter of the cell (S1 Fig). For the unpolarized cells, the patches of high activity are short and there can be severall at the same time. Their duration increases for the intermediate cells. We saw relatively few patches in the highly polarized cells, though previous experiments have shown long, single patches of high activity [24].

Complimentary local feedback loops from the cytoskeleton enhance cell polarity

To determine how feedback loops from the cytoskeleton affect cell polarity, we first incorporated two complementary local feedback loops into our model (Fig 4A; Methods). We included a positive feedback connection between PKB and Ras, noting that elevated PKB leads to increased actin polymerization, which in turn elevates Ras levels [16]. This positive feedback depends on the amount of branched actin in the cell [57] and increases the likelihood that STEN will fire in the vicinity of a protrusion. Because this process depends on the actin cytoskeleton, we restricted its diffusion so that it acts primarily as a local process. Similarly, we added inhibitory feedback between $PI(4,5)P_2$ and Ras to capture the fact that myosin inhibits Ras activation [57]. This was also incorporated as a local loop (Methods).

To assess the relative contributions of these feedback loops, we systematically varied their strengths, simulated the system, and visualized the results as a kymograph matrix. In this matrix, the strength of the branched actin feedback loop increased along the horizontal axis, while the myosin-mediated inhibition increased along the vertical axis (Fig 4B). As previously observed, some simulations produced kymographs where waves translocated laterally following an initial stochastic trigger (e.g., kymograph in magenta). For a fixed myosin feedback strength, increasing actin feedback led to heightened Ras activity along the cell perimeter, generating more and longer-lived patches. Conversely, at a constant actin feedback strength, increasing myosin feedback resulted in reduced activity.

Notably, when both feedback loops reached moderate strengths (e.g., kymograph marked by the black box), we observed stable, persistent patches. In this regime, once the system fired, activity remained elevated without spatial translocation along the membrane. At high positive feedback levels, the entire cell boundary became uniformly active, sustaining elevated activity throughout the simulation, even under strong inhibitory feedback. For moderate positive feedback strengths, increasing the strength of the actomyosin negative feedback loop lowered activity and broke persistent patches into lesser durable patches, reducing polarization.

Kymographs of individual model components (Fig 4C; corresponding to the Ras kymograph marked in green in Fig 4B) revealed that actin and myosin feedback loops aligned with the front (Ras) and rear ($PI(4,5)P_2$) signaling modules, respectively, demonstrating that both loops reinforced polarity in complementary membrane regions.

Plots of the temporal Ras autocorrelation for four different combinations of feedback loop strengths demonstrated that increasing the strength of either feedback loop led to more correlated behavior (Fig 4D). At high actin feedback levels (blue kymograph), the correlation plateaued around 0.35. While stronger myosin feedback resulted in slightly lower values, the overall correlation remained elevated. The presence of a second band, particularly for the

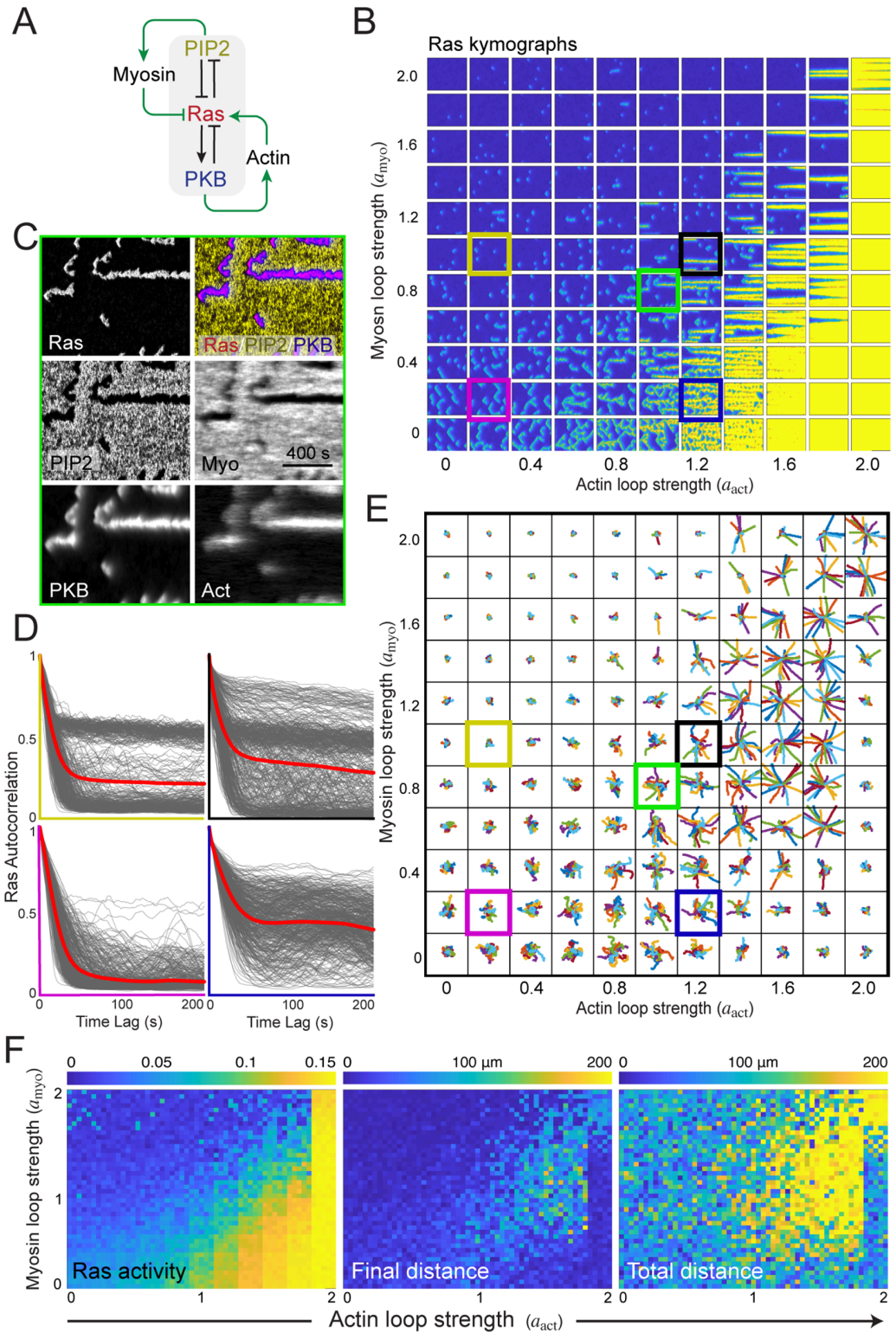

Fig 4. Balancing local positive feedback loops at the front and rear polarize the cell. A. Schematic of the system. The STEN system Fig 2 forms the core. To this, two positive feedback loops are added which primarily work at the front (Ras to PKB, to branched actin, back to Ras) and rear (negative from Ras to PI(4,5)P_2, to myosin, and then negative to Ras.) B. Sample Ras kymographs of the system under varying feedback loop strengths. On the horizontal, the strength of the actin loop (a_{act} in Eq 5) increases from left to right from 0 to 2 at 0.2 steps. On the vertical, there is a similar increase in the myosin feedback strength (a_{myo} in Eq 6), starting at the bottom. Each kymograph shows the activity over 1200 seconds. C. Kymographs of the individual components. This corresponds to the kymograph marked in green in panel

B. D. Temporal correlations for four kymographs from panel B. They are colored (yellow, black, magenta and blue) to match those in panel B. E. Trajectories for systems under the varying feedback strengths. Each condition includes 20 simulations. The strengths of the two feedback loops vary as in panel B. F. Heatmaps showing Ras activity (on a logarithmic scale), total distance traveled, and final displacement for the 2420 simulations (20 simulations for each of the 121 different combinations of the feedback strengths). Each condition is plotted as a 4 by 5 matrix.

https://doi.org/10.1371/journal.pcbi.1013036.g004

upper two cases is indicative of the existence of a second stable equilibrium with high Ras activity; see S2 FigA.

To assess the impact of these feedback loops on cell motility, we used the kymographs (20 per feedback strength combination) to simulate cell movement (Fig 4E; Methods). The results revealed complex biphasic behavior. In the left region of the matrix, where front-feedback strength was low, increasing negative feedback suppressed motion. Conversely, along the bottom of the matrix, where rear feedback was weak, increasing positive feedback enhanced motility. However, in cases where kymographs displayed uniformly high Ras levels (last column), cell motility was inhibited. In these conditions, increasing rear inhibition facilitated efficient migration.

To quantify these effects, we generated heatmaps for total Ras activity, total distance traveled, and net displacement across all simulations (Fig 4F). The heatmaps revealed that increasing actin or myosin feedback led to higher or lower Ras activity, respectively. This trend largely corresponded to total distance traveled, except at extreme Ras activation levels, where high positive feedback and weak negative feedback impaired motility. Finally, the highest net displacement occurred when both feedback loop strengths were elevated.

Local positive and global negative feedback loops reduce the presence of multipolarity

We next explored a model in which actin is involved in complementary positive and negative feedback loops (Fig 5A). The motivation for the positive feedback was consistent with previous findings: increased levels of Ras and PKB lead to greater actin polymerization, which in turn further elevates Ras levels. For the negative feedback, we were inspired by reports indicating that actin polymerization increases membrane and cortical tension, which inhibits signaling at the cell front [54,55].

Kymographs of the system under varying feedback loop strengths (Fig 5B) revealed similar patterns to our previous model: increasing local positive feedback resulted in more and longer-lasting firings, while increasing negative feedback suppressed this response. The optimal polarity — characterized by single, long-lived streaks — occurred when both feedback levels were high (e.g., the kymograph marked in green). Kymographs of the individual components showed that actin-mediated feedback correlated both temporally and spatially with PKB, whereas the tension-mediated negative feedback exhibited temporal correlation with PKB but swept across the cell spatially (Fig 5C).

The autocorrelation patterns in these simulations were similar to those observed in the earlier model, though high-tension feedback induced more pronounced bistability, with clearer distinctions between high and low correlated states compared to the previous model (c.f. Fig 5D vs. Fig 4D, particularly in the kymographs marked by the yellow and red boxes). The impact of the feedback loops on cell motility (Fig 5E and Fig5F) mirrored patterns from the earlier model. We observed a similar biphasic response in scenarios with high positive feedback and low negative feedback, but this effect diminished with small increases in the negative feedback; see S2 FigB.

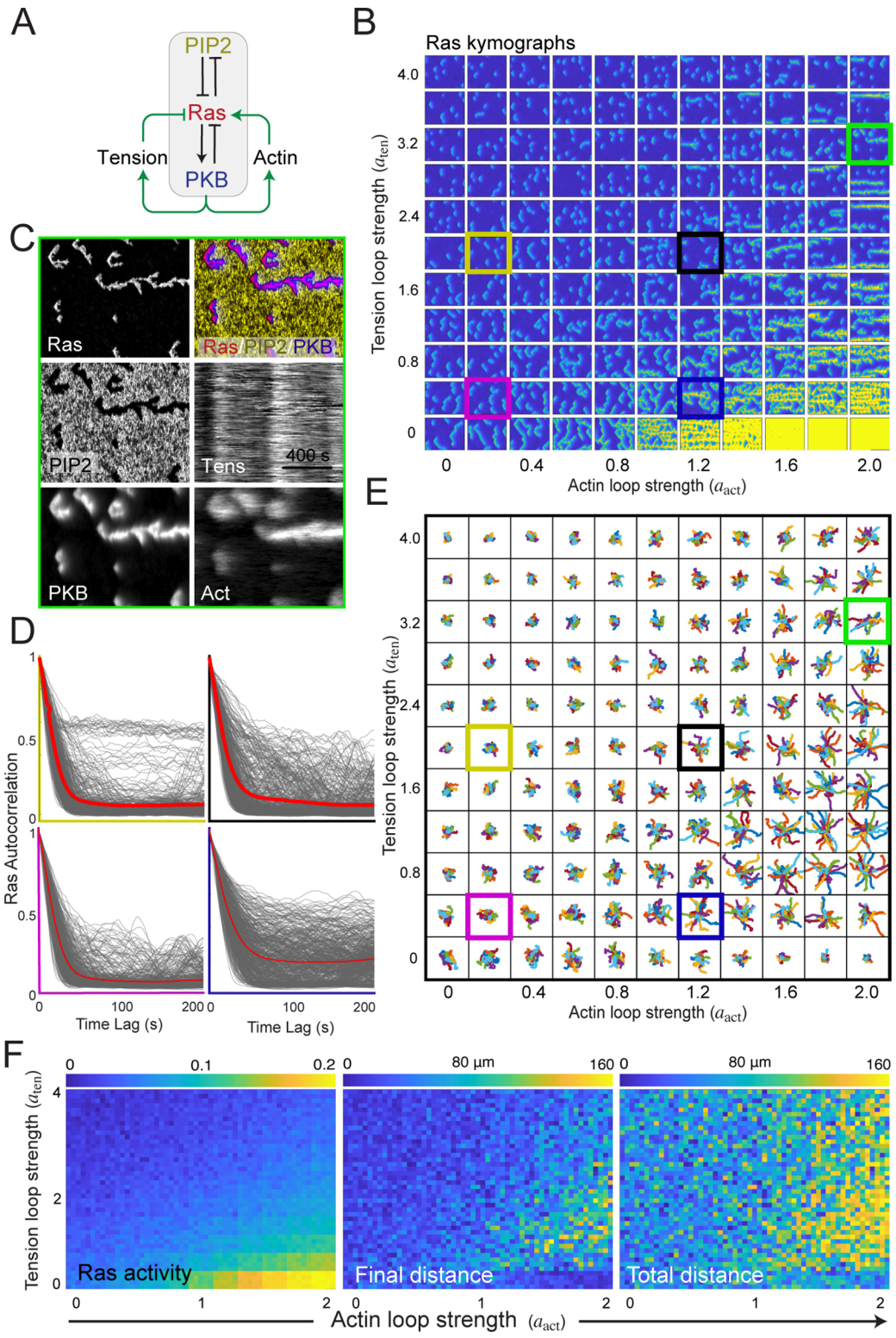

Fig 5. Global inhibition can reduce multipolarity. A. Schematic of the system. The STEN system Fig 2 forms the core. To this, two feedback loops are added that come from protrusions. The local enhancement is as in Fig 4. Additionally, we include a negative feedback loop representative of cortical/membrane tension. B. Sample Ras kymographs of the system under varying feedback loop strengths. As in Fig 4, on the horizontal, the strength of the actin loop (a_{act} in Eq 5) increases from left to right from 0 to 2 in 0.2 steps. On the vertical, the negative feedback strength (a_{ten} in Eq 8) varies from 0 to 4.0 with step size of 0.4. C. Kymographs of the individual components. This corresponds to the kymograph

marked in green in panel B. D. Temporal correlations for four kymographs from panel B. They are color-coded (yellow, black, magenta and blue to match those in panel B. E. Trajectories for systems under the varying feedback strengths. Each condition includes 20 simulations. The strengths are as in panel B. F. Heatmaps showing Ras activity (logarithmic scale), total distance traveled, and final displacement for the 2420 simulations (20 simulations for each of the 121 different combinations of the feedback strengths). Each condition is plotted as a 4 by 5 matrix.

https://doi.org/10.1371/journal.pcbi.1013036.g005

Polarization potential is compromised for local inhibition model

The mechanisms in Figs 4 and 5 can both produce polarized kymographs and sustain persistent, directional migration, provided that the positive and negative feedback loops are properly balanced. To investigate this further, we analyzed several polarization markers (Fig 6).

For example, in Fig 6A, we compared the fraction of cells exhibiting polarized kymographs. Cells modeled using Model 1 (local inhibition; Fig 4) displayed significantly less polarization compared to Model 2 (global inhibition; Fig 5). In both models, polarization predominantly occurred along the diagonal in the branched actin and myosin strength grid. In Model 1, the highest number of polarized cells (15–16) was observed at branched actin strengths of 0.4–0.6 and myosin strengths as low as 0.4, after which polarization declined to 10 or fewer cells. In contrast, Model 2 exhibited a broader range of polarization, with counts between 15 and 20 along the diagonal. Additionally, in Model 2, the polarization region expanded toward the top right corner, suggesting that increasing branched actin strength and global inhibition enhances polarization.

We further compared the models by analyzing the most frequent number of stabilized fronts in each kymograph (Fig 6B). Model 1 produced several instances of the "2-front cell" along the diagonal of increasing branched actin and myosin strength. In contrast, Model 2 exhibited most of its 2-front states in the high branched actin, low global inhibition zone. Notably, achieving a "single front" cell for a given level of positive feedback required higher feedback strengths in Model 1 compared to Model 2. This distinction is reflected in the polarization potential heatmap (Fig 6A), where only cells that predominantly exhibited a single front are included.

Examining the duration of polarity patches, we found a clear positive correlation between the longest persisting patch and the strength of branched actin feedback (Fig 6C). Notably, Model 1 exhibits longer patch durations when branched actin strengths exceed 1.0 compared to Model 2.

To quantify the fraction of time spent in a polarized state, we computed the proportion of simulation time during which cells maintained a single front (Fig 6D). In Model 1, cells remain polarized for approximately 40–60% of the simulation time along the diagonal, indicating increased polarization when feedback strengths are balanced. In Model 2, this effect is less pronounced, as polarization occurs across a broader range of feedback strengths. Extremely high polarization values (≥80%) correspond to conditions in Figs 4 and 5, where Ras activity stabilizes at a persistently high level. In these cases, cells exhibit a single high-activity patch that spans the entire membrane, resulting in the longest patch durations (Fig 6C). However, these cells are not polarized in the traditional sense and are unable to migrate (Figs 4 and 5).

Experimental observations of polarized cells reveal kymographs where the front-associated signals (such as Ras and PIP3) show distinct, persistent regions of activity with minimal angular deviation. Our simulations indicate that both types of negative feedback exhibited this

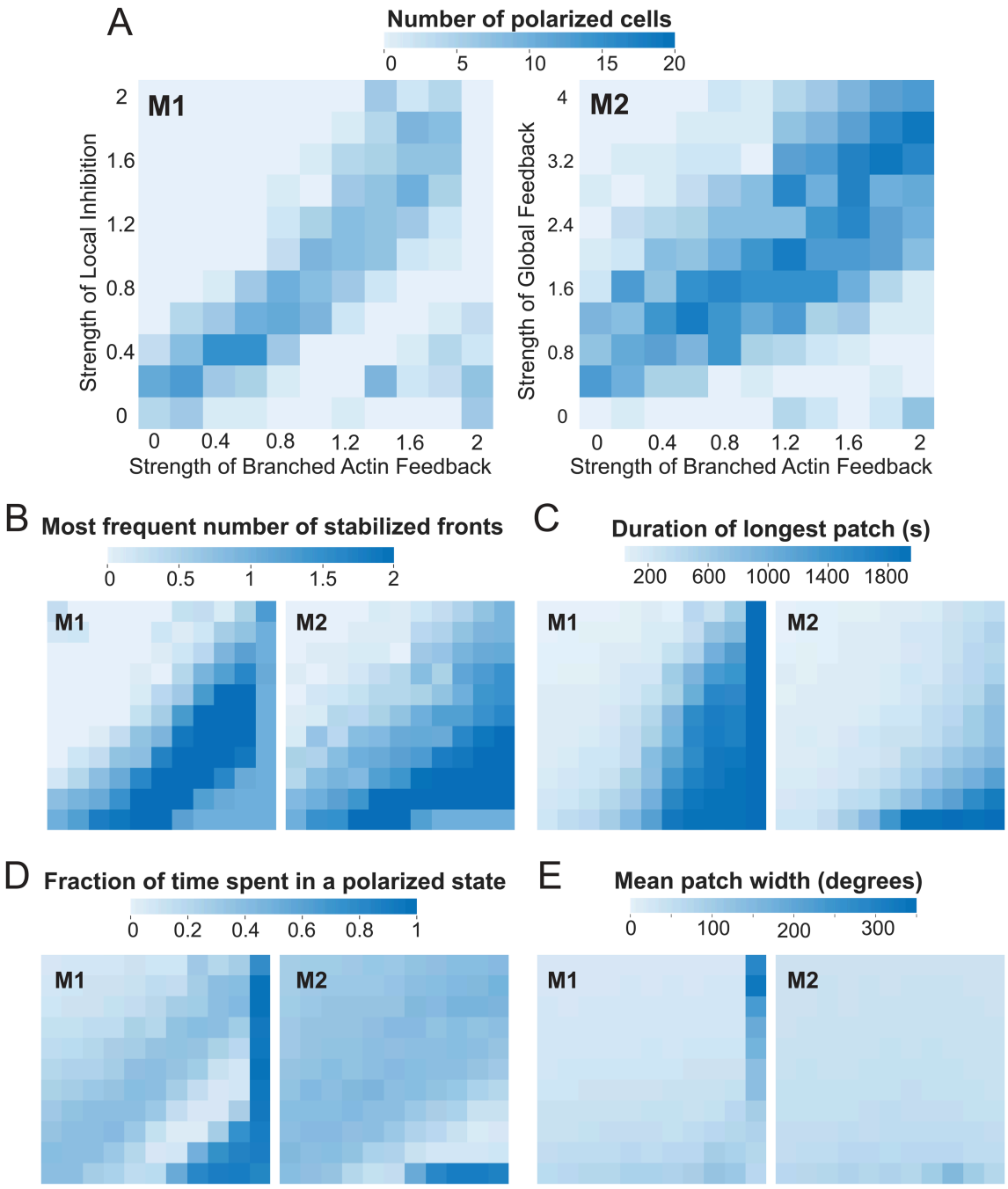

Fig 6. Heatmaps showing polarization potential of the two models. The left column shows statistics for local inhibition through myosin (Model 1; M1), and the right for global inhibition through tension (Model 2; M2). The horizontal axes for both models show strength of Branched Actin (BA) feedback loop (a_{act} in Eq 5) ranging from 0 to 2.0, in 0.2 intervals. For M1, the vertical axis is the strength of myosin feedback (a_{myo} in Eq 6) ranging from 0 to 2 in intervals of 0.2; for M2, it is the strength of the global inhibition loop, (a_{ten} in Eq 8) ranging from 0 to 4 in intervals of 0.4. The difference in these ranges accounts for differences in inhibitor levels in the two systems such that strength of negative feedback on STEN stayed the same. A. Number of polarized cells in a population size of $n = 20$ cells. In each simulation, patches are filtered to include only those that have more than 50 pixels and the ellipse fit to the patch made an angle of less than 30° with respect to the time axes. At each time step, the number of filtered patches was quantified. B. The most frequently appearing number of patches at any point in time. C. Length of the longest patch, in seconds. D. Fraction of time spent in a polarized state. This uses the data from panel B to obtain the time points for which there is a single front. The sorting criteria were based on outcomes from panels B–D, where "polarized" cells exhibited a single front as their most frequent state and the mean patch width was less than 60°. E. Mean path width, in degrees.

https://doi.org/10.1371/journal.pcbi.1013036.g006

behavior, although the more diffusive global inhibitor demonstrated it with greater consistency, suggesting a more robust mechanism. Additionally, we simulated a model incorporating both feedback loops while varying the strengths of global positive feedback and local negative feedback (S3 Fig). As anticipated, these simulations demonstrated that the two forms of negative feedback can complement each other. However, the limited number of combinations that resulted in polarized cells suggests a lack of robustness in the system.

Local, but not global inhibition captures the behavior of cells under perturbation

While both local and global inhibition models generate polarization across different parameter spaces, we further examined their biological relevance by testing their ability to replicate perturbation experiments. These experiments involve overexpression or underexpression of key molecules in the signaling pathway, as well as optogenetic modulation through laser-induced recruitment or depletion of proteins in wild-type cells. Perturbations targeting different polarization loops have been extensively studied in *Dictyostelium* [24]. Here, we analyze similar perturbations in neutrophils, which exhibit analogous responses, emphasizing the universality of polarization mechanisms.

A wild-type polarized neutrophil is characterized by a flared-out front and a narrow tail at the back. Actin fluorescence is observed at both ends: branched actin at the front and actomyosin-rich, contractile structures at the rear.

Perturbations are introduced at time zero, with cellular responses tracked over time. In the first experiment, Ras activity was globally increased by activating a 488 nm laser to recruit cytosolic KRas4B G12V to the cell periphery (Fig 7A). Before recruitment, both cells exhibited single, stable fronts and directional movement (S4 Video). In the second frame, the top cell changed direction but retained its front. Following Ras recruitment, multiple sites along the membrane became active upon cell-cell contact, ultimately leading to a two-front phenotype in the top cell. In silico, Ras upregulation produced different outcomes depending on the polarization model. In the local excitation-local inhibition model, increased Ras induced widespread, persistent activity across the membrane, disrupting polarity. In contrast, in the local excitation-global inhibition model, Ras enhancement reinforced localization of a single persistent patch, promoting stronger polarization.

Next, we tested the effects of PIP2 depletion by globally recruiting cytosolic INP54P to the membrane using a 488 nm laser (Fig 7B and S5 Video). Following recruitment, the actomyosin tail disappeared, and the leading edge expanded. The cell developed a second front at its former rear, with no reformation of the actomyosin tail. In silico, PIP2 depletion had distinct effects in each model. In the local excitation-local inhibition framework, its impact resembled that of Ras upregulation, leading to loss of polarity and widespread activity. In the local excitation-global inhibition model, polarization decreased due to the formation of broader, less persistent, and more dispersed waves.

The first two perturbations targeted components of the signal transduction excitable network (STEN). In the third experiment, we inhibited Arp2/3-mediated branched actin formation using CK666 (Fig 7C and S6 Video), directly disrupting the positive feedback loop between the cytoskeleton and STEN. Following inhibition, the leading edge collapsed, while the actomyosin-rich rear enlarged and intensified in fluorescence. Since actin could no longer form branched networks, excess monomeric actin accumulated at the rear, reinforcing actomyosin structures. The resulting loss of cytoskeletal feedback disrupted front persistence and patch localization in both models, severely impairing motility.

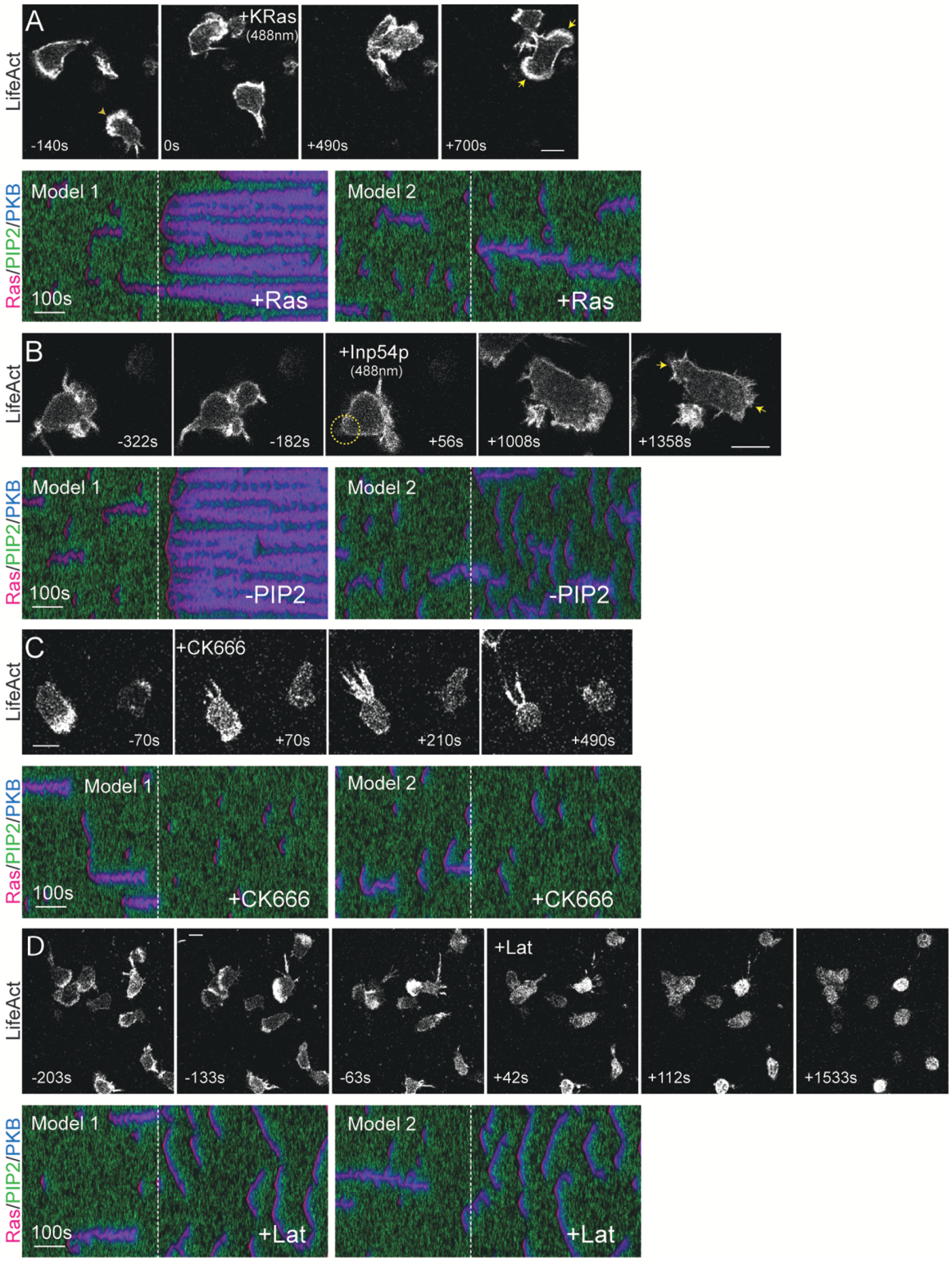

Fig 7. Perturbations that impact front and back polarity. (A-D) Differentiated neutrophils with F-actin-rich fronts (denoted by LifeAct-miRFP703) were imaged over time, and their shape and displacement were measured. Corresponding perturbations were simulated using Model 1 (local inhibition) and Model 2 (global inhibition), with the first 400 seconds showing STEN activity before effector recruitment (A–B) or drug addition (C–D), and the last 500 seconds showing STEN activity post-effector recruitment (A–B) or drug addition (C–D). The three colors in the kymograph represent Ras (Red), PKB (Blue), and PIP2 (Green). A. A 488 nm laser was switched on at frame 50 to globally recruit cytosolic CRY2PHR-mCherry-KRas4B G12V ΔCAAX to the cell periphery, increasing Ras activity

and activating the STEN network. B. A 488 nm laser was switched on at frame 47 to globally recruit cytosolic CRY2PHR-mCherry-INP54P to the cell periphery, reducing PIP2 levels, which serves as the back molecule in STEN in both models. C. Differentiated neutrophils were pre-treated with 50 μM CK666 to inhibit branched actin (denoted by LifeAct-miRFP703), turning off its positive feedback. D. Cells were pre-treated with 5 μM Latrunculin B to completely remove actin polymerization (denoted by LifeAct-miRFP703), turning off both positive and negative feedback. Scale bar: 5 μm.

https://doi.org/10.1371/journal.pcbi.1013036.g007

Finally, to abolish all cytoskeletal feedback, we treated cells with Latrunculin B, an inhibitor of actin polymerization (Fig 7D and S7 Video). Wild-type cells with well-defined fronts and tails began to round up upon drug exposure. The actomyosin tail and leading edge retracted, and after prolonged treatment, cells became entirely spherical. In silico, removal of both positive and negative feedback loops caused both models to revert to the basal STEN phenotype observed in Fig 2, underscoring that the observed differences arise solely from cytoskeletal feedback interactions.

PIP5K generates local and global inhibition

Our simulations demonstrate that global inhibition provides a more effective means of polarizing cells. However, perturbation experiments in both *Dictyostelium* [24] and neutrophils (Fig 7) are more closely satisfied with the local inhibition model. Though it is likely that cells combine both forms of inhibition, recent experiments in *Dictyostelium* suggest that a third mechanism may be in action [59].

A core component of the STEN network is that PIP2 and Ras form a mutually-inhibitory positive feedback loop [57]. Recently, Deng *et al*. demonstrated that Ras-mediated regulation of PIP5K can further amplify this loop leading to cell polarization [59]. They observed that, in resting cells, PIP5K was uniformly distributed, while Ras activity was minimal. Spontaneous PIP5K displacements disrupted this symmetry, activating Ras and downstream signaling, including PI3K. PIP5K knockouts increased Ras-PI3K activation and cortical wave formation, affecting cell protrusion and migration. Conversely, low PIP5K overexpression promoted polarity, highlighting its role as a key regulator.

We incorporated these findings into our model (Methods; Fig 8A.) The model assumes that PIP5K is in two states: membrane-bound and unbound, with differing diffusion characteristics (low and high diffusivity, respectively). Because RasGTP facilitates the release of PIP5K, in regions of high Ras activity, PIP5K is released and diffuses away. In these regions, the absence of PIP5K inhibits PI(4,5)P_2 production which hinders further Ras inhibition. Thus, this acts as a local positive feedback loop (high Ras → locally low PIP5K → low PIP2 → high Ras). On the other hand, the diffusion of PIP5K away from the region of high Ras activity also acts as global inhibitor (high Ras → high PIP5K away → high PIP2 away → low Ras).

We examined PIP5K's inhibitory role and its potential contribution to myosin-mediated local inhibition by computing the activation threshold of the excitable system under a mean-field assumption (no diffusion or noise; S4 Fig). In this plot, we take as the baseline the system of Fig 4 with high positive feedback ($a_{act} = 1$) and moderate level of local negative feedback ($a_{myo} = 0.3$). The level of PIP5K is set at one, where excitable behavior is observed. Lower values of PIP5K make the threshold smaller, eventually making the equilibrium unstable (the dotted line in S4 FigC, at PIP5K levels around 0.6). Further lowering PIP5K leads to a new high Ras set point (the high region at the left of the graph). On the other hand, increasing the levels of PIP5K above one raises the activation threshold (i.e. the cell becomes less active) but remains excitable. The inset shows that there is a biphasic peak when the normalized PIP5K

level is close to 4. Thus, as expected, greater PIP5K leads to more PIP2, hence less Ras and less active cells.

The analysis above shows that PIP5K can act as a local enhancer of activity; however, it does not capture the spatial effect of the regulated PIP5K. In simulations of unperturbed cells, the two PIP5K states exhibited distinct distributions (Fig 8B). Bound PIP5K was depleted at the Ras-active front but enriched at the periphery and rear, with limited spatial spread owing to low diffusion. Unbound PIP5K appeared at the front (i.e. regions of high Ras) but dissipated rapidly. Increased bound PIP5K regions coincided with the termination of unbound PIP5K waves. Bound and unbound PIP5K concentrations remained complementary, maintaining a constant total concentration over time (Fig 8C). The spatial profile across the cell at a given time (white dotted line in the kymograph) showed a drop in bound PIP5K concomitant with regions of elevated Ras activity.

The simulation of Fig 8B–8D shows primarily a single Ras streak that is suggestive of polarized cells. In this simulation, we assumed that both bound and unbound states contributed equally to $PI(4,5)P_2$ production. However, we also considered the possibilities that only bound or unbound PIP5K was active and considered situations of varying levels of branched actin and with- or without myosin (Fig 8E). In simulations in which PIP5K was active only in the bound state, this inhibition had relatively small effect on the wave patterns (top row of Fig 8F). Activity increased as the levels of branched actin rose. Moreover, persistent patches did appear with high levels of high branched actin and in the presence of myosin inhibition.

When we considered unbound PIP5K inhibition alone (middle row of Fig 8F), the level of Ras activity was considerably lower than in the bound case and persistent patches were seen only under high branched actin levels and with myosin present. However, when both states of PIP5K provided PIP2-mediated Ras inhibition (bottom row of Fig 8F), the polarization was better, particularly in the high branched actin and myosin case when a single, persistent streak was seen.

Discussion

Many early models of chemoattractant-induced polarization were based on the two feedback loops that mirror the classical Turing/Meinhardt-Gierer model of pattern formation: (1) a local self-enhancing reaction and (2) a long-range (global) inhibitor to counterbalance it [60,61]. The first arises when activation occurs at the membrane or cortex, while inhibition diffuses freely across the membrane or cytosol. Together, these processes generate diffusion-driven stable patterns and recreate front/back polarity of motile cells.

Positive feedback from the cytoskeleton to the signaling network plays a crucial role in establishing polarization by amplifying signaling activity and creating a spatial memory of prior excitations, thereby increasing the likelihood that future triggers will activate those regions. This process leads to persistent excitation in specific domains of the cell membrane, which is essential for directional migration. In our models, positive feedback amplifies Ras activity by enhancing its production rate. This positive feedback has a longer lifetime than that of the signaling network, establishing a locational memory following protrusion formation. However, if this memory does not trigger further firings, the effect of the positive feedback eventually decays, causing the memory to fade — *Dictyostelium* cells exhibit a persistence time on the order of several minutes.

Positive feedback alone, however, is insufficient to establish a polarized cell. Cells relying solely on positive feedback often develop multiple stabilized fronts and, in extreme cases, become hyperactive (bottom row, Fig 4B and 5B). To counteract this, models have typically

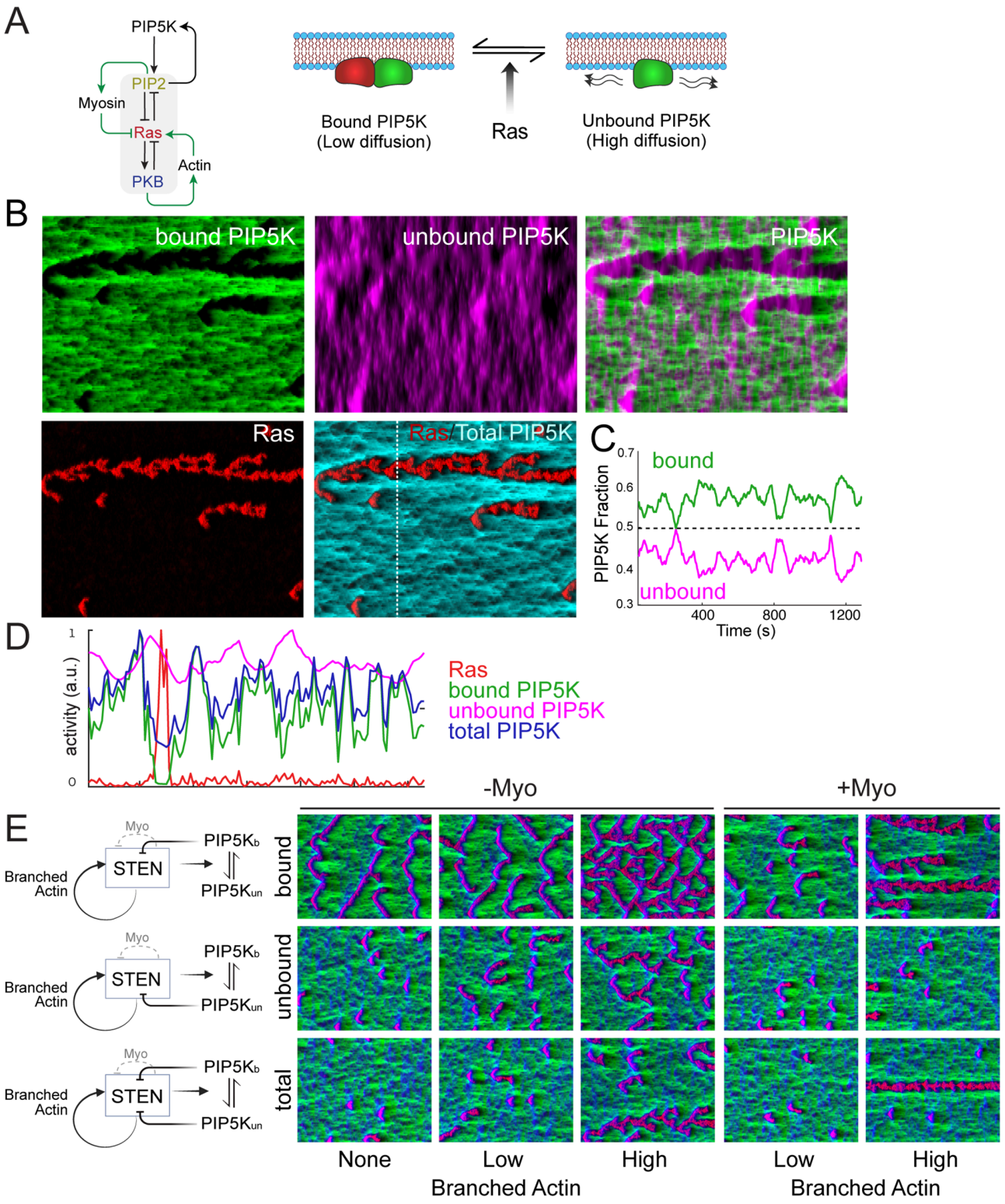

Fig 8. Dynamic partitioning mechanism of PIP5K increases polarization potential. A. Scheme of PIP5K action on the STEN excitable network. Ras activity releases membrane-bound PIP5K which allows it to diffuse easily away from protrusive regions. B. Simulation in which bound and unbound PIP5K contributed to PIP2 formation. In the simulation, local positive feedback ($a_{act} = 1$) and local negative feedback ($a_{myo} = 0.4$) were used. The total time was 1200 seconds. C. Fraction of bound and unbound PIP5K during the time course of the simulation of panel B. Each time point shows the sum of the individual states across the whole field. D. Spatial distribution of the various components at one time point (marked by the white line in panel B. E. Schematics and simulation kymographs illustrating the effects of different PIP5K contributors to inhibition: inhibition via bound PIP5K (**bound**),

unbound PIP5K (**unbound**), and an equal contribution from both forms (**combined**). In the simulation grid, rows correspond to different strengths of the positive feedback loop: $a_{act} = 0$ (no branched actin), $a_{act} = 0.2$ (low branched actin), and $a_{act} = 0.8$ (high branched actin) and of the local negative feedback strength: $a_{myo} = 0$ (-Myo) and $a_{myo} = 0.4$ (+Myo). This arrangement applies to all simulations in the grid except for the bottom-right corner (high branched actin, +Myo), where the highly polarized phenotype corresponds to $a_{act} = 1$ and myosin strength $a_{myo} = 0.6$.

https://doi.org/10.1371/journal.pcbi.1013036.g008

incorporated global inhibition to ensure that, once a front forms, the rest of the cell remains quiescent [62–66]. Models based on this local positive, global negative feedback paradigm successfully achieve polarization in both unstimulated cells and those sensing a chemoattractant gradient. In Shi et al. [38], we demonstrated that this mechanism functions within an excitable network (EN) context, guiding movement for cells in gradients and enabling persistent random migration in their absence. The simulations in Fig 5, based on this local positive and global negative feedback paradigm, confirm that this model works well. Experiments suggest that the fast global inhibition required by these models could be achieved through the membrane or cortex. This inhibition typically originates from the strain caused by protrusive forces at the cell's front, which makes it more difficult for new protrusions to form elsewhere [53–55].

In one of the earliest computational studies on migratory cell polarization, Meinhardt proposed that a third component was needed: a local, longer-lived antagonist of the activator that destabilizes high-activity regions, allowing new ones to form [67]. The existence of this local inhibition has not been tested thoroughly, nor has there been much evidence for it experimentally. Recently, experiments showed that increasing RasGAP in cells with initially high Ras activity enhanced polarity [56]. This finding is somewhat puzzling, as RasGAP inhibits RasGTP, thus acting as a negative modulator of activity (S5 Fig). Front-mediated global inhibition fails to account for these observations. More recently, Kuhn et al. identified distinct positive and negative components of cytoskeletal inhibition by perturbing polarized cells [24]. They found that negative feedback originates from actomyosin, establishing a back-mediated inhibition system that localizes at the cell's rear. Thus, actomyosin enhances polarization by suppressing protrusions at the back. This provides a local inhibitory mechanism.

To understand these findings within our framework, we note that in our excitable network, which models Ras, PIP2, and PKB as the front, back, and refractory components, respectively, Ras deactivation (RasGTP to RasGDP) is governed by its degradation rate. Thus, GAP directly influences Ras degradation in our equations (Methods). In the model of Fig 4, local inhibition was used to capture these GAP-related experiments, incorporating actomyosin as a local inhibition mechanism originating from PIP2 (back). This mechanism increases Ras degradation more at the rear (where PIP2 levels are high) than at the front (where PIP2 levels are low). In the GAP recruitment experiments, a global increase in GAP led to an overall reduction in Ras activity and more polarized cells [56]. However, simulations showed that globally altering Ras degradation in the excitable network failed to enhance polarization (Fig 4B). This enhancement only occurred when front-mediated local positive feedback was counterbalanced by actomyosin-driven local negative feedback.

While the local inhibition model successfully captured Ras perturbation experiments, it failed to polarize cells robustly — defined as maintaining a single persistent front while suppressing activity elsewhere along the cell perimeter (Fig 4). Even under optimal feedback strengths, the model frequently stabilized two fronts instead of one (Fig 6). Moreover, compared to global inhibition, local inhibition proved to be a weaker mechanism at higher levels of positive feedback — in fact, bifurcation diagrams of the two schemes show greatly reduced bistability for the global inhibition method when compared to local inhibition (S2 Fig). Whereas global inhibition effectively maintained confined patches of activity and often

supported polarization at elevated branched actin levels, local inhibition, at the same mean inhibition strength, became increasingly hyperactive as branched actin strength increased. Eventually, at the highest levels of branched actin feedback, the entire cellular perimeter remained persistently active, resembling conditions observed in the absence of inhibitory feedback (cf. right column vs. bottom row of Fig 4B). This highlights the critical role of spatial delocalization and long-range negative feedback in establishing stable polarization.

To bridge the gap between a model that captures experimental perturbations and one with strong polarization potential, we propose here a novel scheme based on the dynamic regulation of PIP5K by Ras (Fig 9, [59,68]). Recent experiments have shown that PIP5K, a membrane-bound Ras inhibitor, remains confined to the membrane, does not enter the cytosol, and diffuses slowly across the membrane [59]. Based on these experiments, we incorporated into the model PIP5K, which exists in two states: a slow-diffusing bound state (S6 Fig and S8 Video) and a highly diffusible unbound state (Fig 8A). The total PIP5K in the system is conserved, but the two states coexist dynamically. We expected that high Ras activity at the front causes PIP5K to unbind, allowing it to diffuse freely. Binding sites at the rear of the cell capture this unbound PIP5K; thus, it accumulates at the rear. Because PIP5K enhances PIP2 production, and the latter inhibits Ras, this creates an effective positive feedback loop at sites of high Ras activity. On the other hand, since PIP5K accumulates at the rear, it increases PIP2 production there, thereby strengthening the inhibition at the rear. Thus, PIP5K acts both as a (front) local enhancer and a (rear) local inhibitor.

Through simulation, we tested this model under various possibilities (Fig 8). Though experiments have shown that PIP5K binding is regulated, they leave a number of questions open as to how this may contribute to polarization. One possibility is that, following unbinding, PIP5K transiently inhibits Ras, interfering with the branched actin positive feedback loop and thereby disrupting persistent patches, which reduces cellular polarization (middle row of Fig 8E). Therefore, if inhibition is solely accomplished by unbound PIP5K, cells would not polarize. Conversely, if inhibition comes solely from the bound state, which is localized at the

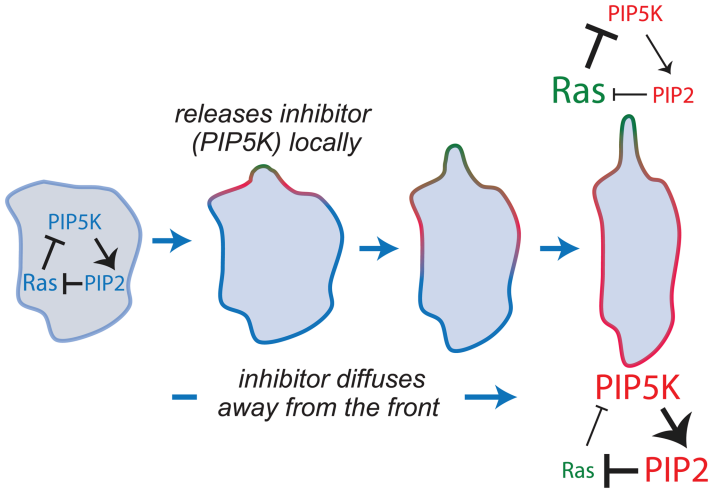

Fig 9. Mechanism for Ras-mediated regulation of PIP5K. This diagram illustrates how localized activation of Ras induces the release of PIP5K from the membrane. Subsequently, unbound PIP5K diffuses away from the site of Ras activity, leading to a reduction in local levels of $PI(4,5)P_2$, which diminishes its inhibitory effects on Ras. This results in an increase in Ras activity in the vicinity. Conversely, as PIP5K diffuses, it enhances $PI(4,5)P_2$ levels in areas further away, inhibiting Ras activity in those regions. Together, these dynamics contribute to cellular polarization.

https://doi.org/10.1371/journal.pcbi.1013036.g009

rear, it is ineffective due to its highly localized nature and limited diffusion, preventing it from suppressing secondary and tertiary front formations (top right simulation of Fig 8E). Simulations showed that the most polarized cells were observed when both PIP5K states inhibit Ras and that positive feedback from branched actin is required (bottom right panel of Fig 8E).

We also simulated the system under conditions where myosin is absent so that the only inhibitory mechanism is through PIP5K (-Myo simulations of Fig 8E). These simulations showed that, with positive feedback and both states of PIP5K inhibiting Ras, cells could polarize, but not as efficiently as with the myosin contribution. These simulations recapitulated experimental findings [59]. Thus, we conclude that the combination of branched actin positive feedback, back-mediated myosin inhibition, and PIP5K dynamic partitioning leads to highly polarized cells. Notably, by having both states act as inhibitors, PIP5K achieves both local and global inhibition. When paired with back-mediated myosin inhibition, dynamic partitioning enhances negative feedback at the back, as both PIP5K states inhibit Ras activation while promoting PIP2 production. The high diffusivity of unbound PIP5K enables a broader range of inhibition, making it functionally more global than myosin-based negative feedback alone.

Though most of our models are motivated by experiments in *Dictyostelium*, there is plenty of evidence that the same combination of excitable systems is active in other cell types, including neutrophils [69], RAW 264.7 cells macrophages [56,59,70,71], and epithelial cells [72].

In conclusion, our study suggests that the combination of local positive feedback and global inhibition is needed to provide robust polarization — this fits the long-standing framework of many polarization models. However, we also show that local and not global inhibition allows us to match the experimentally observed perturbations more accurately. Our results suggest that cells rely on both mechanisms. Our PIP5K-based model demonstrates an elegant way that a single protein can perform both the local enhancement at the front and local inhibition at the rear.

Materials and methods

Reaction-diffusion equations: STEN

The simulations are based on a previously described model in which three interacting species — RasGTP (Ras), PI(4,5)P_2 (PIP2), and Protein Kinase B (PKB) — form an excitable network [16]. In this model, Ras and PIP2 are complementary: high Ras activity corresponds to low PIP2 levels and vice versa, a balance achieved through mutually inhibitory interactions that generate a positive feedback loop, characteristic of excitable networks [57]. PKB serves as the refractory species, activated by Ras but providing slow negative feedback [16,73]. The concentrations of these molecules are governed by stochastic reaction-diffusion partial differential equations:

$$\frac{\partial[\mathrm{Ras}]}{\partial t} = -\left(a_1 + a_2[\mathrm{PKB}]\right)[\mathrm{Ras}] + \frac{a_3}{1 + a_4^2[\mathrm{PIP2}]^2} + a_5 + w_{\mathrm{Ras}} + D_{\mathrm{Ras}}\nabla^2[\mathrm{Ras}] \quad (1)$$

$$\frac{\partial[\mathrm{PIP2}]}{\partial t} = -\left(b_1 + b_2[\mathrm{Ras}]\right)[\mathrm{PIP2}] + b_3 + w_{\mathrm{PIP2}} + D_{\mathrm{PIP2}}\nabla^2[\mathrm{PIP2}] \quad (2)$$

$$\frac{\partial[\mathrm{PKB}]}{\partial t} = -c_1[\mathrm{PKB}] + c_2[\mathrm{Ras}] + w_{\mathrm{PKB}} + D_{\mathrm{PKB}}\nabla^2[\mathrm{PKB}]. \quad (3)$$

In each of these equations, the final term represents the diffusion of the species, where D_* is the respective diffusion coefficient and ∇^2 is the spatial Laplacian. The second-to-last terms represent molecular noise. Our model assumes a Langevin approximation in which the size

of the noise is based on the reaction terms [74]. For example, in the case of PKB, the noise is given by

$$w_{\mathrm{PKB}}(t) = \alpha\sqrt{c_1[\mathrm{PKB}] + c_2[\mathrm{Ras}]}\, w(t)$$

where $w(t)$ is a zero-mean, unit-variance Gaussian, Brown-noise process. In the simulations, the size of this noise was adjusted with the empirical parameter α.

The system is largely robust to parameter changes, in that variations from the nominal values continue to give rise to excitable behavior [56]. To test this, we note that excitable behavior arises from the stochastic crossing of a threshold that is determined by the nullclines of the differential equations. To measure the level of robustness, we varied each of the parameters $a_1, \ldots, a_5$, $b_1, \ldots, b_3$, c_1, and c_2 from their nominal values and computed the size of the threshold. Some, like a_2, b_2, and c_1, are quite robust, allowing large changes in either direction. Others allow large changes only in one direction.

Parameter values, given in Table 1, were selected to replicate experimental observations regarding excitable activities, such as the number of firings per unit time and wave propagation. Additionally, the choice was based on certain considerations. The diffusion was set such that the inhibitor diffused slightly faster than the activator. With these parameters, we observed wide waves that traveled large distances but did stop, and also occasionally we would get propagating waves, similar to those seen in Latrunculin-treated cells [75].

Reaction-diffusion equations: Polarization

In addition to the STEN dynamics described above, we incorporate two additional terms related to cell polarization (see Fig 1). The first of these feedback loops captures the influence of actin on polarity. Experimentally, increasing the assembly of branched actin has been shown to activate the Ras/PI3K signaling pathway, which is essential to promote the cell's "front state," leading to protrusion and movement [24]. Conversely, inhibiting branched actin results in an increase in cortical actin assembly and a strong suppression of Ras/PI3K activation, thereby promoting the 'back-state' of the cell. We represent the local abundance of branched actin by the variable P_{act}. Furthermore, we assume that STEN regulates P_{act} through the concentration of PKB, as previous studies have shown that the synthetic recruitment of

Table 1. STEN reaction-diffusion parameter values.

Parameter	Value	Units
a_1	0.0333	s^{-1}
a_2	0.7125	$\mu M^{-1}s^{-1}$
a_3	0.2850	s^{-1}
a_4	400	μM^{-1}
a_5	1.28×10^{-4}	$\mu M\, s^{-1}$
b_1	0.0036	s^{-1}
b_2	0.4920	$\mu M\, s^{-1}$
b_3	533.5	$\mu M^{-1}s^{-1}$
c_1	0.0186	s^{-1}
c_2	0.2160	s^{-1}
D_F	0.0075	$\mu m^2 s^{-1}$
D_B	0.0075	$\mu m^2 s^{-1}$
D_R	0.225	$\mu m^2 s^{-1}$
α	0.091	

https://doi.org/10.1371/journal.pcbi.1013036.t001

PKB to the membrane enhances actin polymerization [16]. Thus, we have:

$$\frac{\partial[P_{\text{act}}]}{\partial t} = -p_1[P_{\text{act}}] + p_2[\text{PKB}] + w_{P_{\text{act}}} + D_{P_{\text{act}}}\nabla^2[P_{\text{act}}] \tag{4}$$

This component subsequently enhances Ras activity by modifying the production term of RasGTP:

$$\frac{a_3}{1 + a_4^2[\text{PIP2}]^2} + a_5 \longrightarrow \left(\frac{a_3}{1 + a_4^2[\text{PIP2}]^2} + a_5\right) \times (1 + a_{\text{act}}[P_{\text{act}}]) \tag{5}$$

This establishes a positive feedback loop in which an increase in Ras leads to elevated PKB levels, which in turn enhances actin assembly, further promoting Ras production. This actin-mediated feedback was used in the simulations of Figs 4, 5, and 8.

We also consider two inhibitory mechanisms. The first, used in the simulations of Fig 4, highlights the role of the acto-myosin network. Myosin II assembly leads to an immediate increase in Ras/PI3K activation, which enhances the cell's sensitivity to chemotactic stimuli and promotes front-state behaviors, such as protrusion [24]. Conversely, myosin II disassembly reduces actin contraction at the cell's rear, preventing the stabilization of the back-state. Together, this forms a feedback loop in which Ras/PI3K signaling promotes myosin II disassembly, and reduced myosin levels further enhance Ras/PI3K activation. We represent this interaction using a rear component, (P_{myo}), with its concentration regulated by:

$$\frac{\partial[P_{\text{myo}}]}{\partial t} = -p_3[P_{\text{myo}}] + p_4[\text{PIP2}] + w_{P_{\text{myo}}} + D_{P_{\text{myo}}}\nabla^2[P_{\text{myo}}].$$

The input to this is PIP2, which represents a rear contribution [56]. These terms modify the components of the RasGTP equation related to hydrolysis:

$$(a_1 + a_2[\text{PKB}]) \longrightarrow (a_1 + a_2[\text{PKB}]) \times (1 + a_{\text{myo}}[P_{\text{myo}}]). \tag{6}$$

Note that this scheme represents local inhibition (Fig 1). More importantly, the feedback loop operates through the rear signal PIP2. Thus, while the net effect is to inhibit the front component (Ras), it achieves this by closing a positive feedback loop on the rear signal.

In the second inhibitory mechanism, protrusions are assumed to increase tension, which consequently reduces Ras activity [55]. This model is similar to that of P_{myo}, but because tension acts globally, we represent it as follows:

$$\frac{\partial[P_{\text{ten}}]}{\partial t} = -p_5[P_{\text{ten}}] + p_6 \times \text{mean}([\text{PKB}])$$

The mean value averages the concentration around the cell, representing a system in which the effect is global. Tension acts to inhibit Ras production, and we considered scenarios in which either hydrolysis is enhanced:

$$(a_1 + a_2[\text{PKB}]) \longrightarrow (a_1 + a_2[\text{PKB}]) \times (1 + a_{\text{ten}}[P_{\text{ten}}]). \tag{7}$$

or the production of Ras is inhibited:

$$\frac{a_3}{1 + a_4^2[\text{PIP2}]^2} + a_5 \longrightarrow \left(\frac{a_3}{1 + a_4^2[\text{PIP2}]^2} + a_5\right) \times \frac{1}{1 + a_{\text{ten}}[P_{\text{ten}}]} \tag{8}$$

Because of the spatial nature of this negative feedback, we refer to this as the global-inhibition mechanism (see Fig 1).

Parameter values for these various feedback loops can be found in Table 2.

Incorporating PIP5K into the model

In addition to the models described above, which differ regarding the spatial resolution of the inhibitor, we also considered a third class of model in which PIP5K is found in both membrane-bound (low diffusion) and unbound (high diffusion) forms and that this conversion is mediated by Ras. This model is motivated by recent experiments [59] that show how the mutually inhibitory localization of PIP5K and Ras activities, mediated through a dynamic partitioning mechanism [68].

This model considers PIP5K in two states: bound to the membrane ($PIP5K_b$ and $PIP5K_{un}$) with Ras helping to release the bound form:

$$\frac{\partial[\mathrm{PIP5K_b}]}{\partial t} = -p_7 \frac{[\mathrm{Ras}]^2}{1+p_9^2[\mathrm{Ras}]^2}[\mathrm{PIP5K_b}] + p_8[\mathrm{PIP5K_{un}}] + D_{\mathrm{PIP5K_b}}\nabla^2[\mathrm{PIP5K_b}].$$

$$\frac{\partial[\mathrm{PIP5K_{un}}]}{\partial t} = p_7 \frac{[\mathrm{Ras}]^2}{1+p_9^2[\mathrm{Ras}]^2}[\mathrm{PIP5K_b}] - p_8[\mathrm{PIP5K_{un}}] + D_{\mathrm{PIP5K_{un}}}\nabla^2[\mathrm{PIP5K_{un}}].$$

The effect of PIP5K is to increase the production of PIP2 by increasing parameter $b_3 \mapsto b_3(1 + a_{\mathrm{pip5k}}[\mathrm{PIP5K}])$ in the model. We considered three possibilities for describing how this takes place; either through bound, unbound, or all PIP5K . These simulations also incorporated the effects of branched actin and myosin feedback loops. Parameter values are given in Table 3.

Table 2. Polarization loops parameter values.

Parameter	Value	Units
p_1	0.0125	$\mu M^{-1}s^{-1}$
p_2	0.0125	$\mu M^{-1}s^{-1}$
$D_{P_{act}}$	0.0075	$\mu m^2 s^{-1}$
a_{act}	0.2–2.0	μM^{-1}
p_3	0.0125	$\mu M^{-1}s^{-1}$
p_4	0.0125	$\mu M^{-1}s^{-1}$
$D_{P_{myo}}$	0.0013	$\mu m^2 s^{-1}$
a_{myo}	0.4–4.0	μM^{-1}
p_5	0.0125	$\mu M^{-1}s^{-1}$
p_6	0.0125	$\mu M^{-1}s^{-1}$
a_{ten}	0.2–2.0	μM^{-1}

https://doi.org/10.1371/journal.pcbi.1013036.t002

Table 3. PIP5K loop parameter values.

Parameter	Value	Units
p_7	1600	s^{-1}
p_8	0.05	s^{-1}
p_9	0.025	μM^{-1}
D_{PIP5K_b}	6.25×10^{-4}	$\mu m^2 s^{-1}$
$D_{PIP5K_{un}}$	0.00125	$\mu m^2 s^{-1}$
a_{pip5k}	4	μM^{-1}

https://doi.org/10.1371/journal.pcbi.1013036.t003

Simulating cell movement

To simulate cell movement, we adopted the procedure outlined previously [76]. In brief, PKB activity along the cell perimeter (in a one-dimensional simulation) was thresholded to generate a force normal to the cell surface. The vector sum of these forces around the perimeter was used to calculate a net force, which was scaled to fall within the range of experimentally observed protrusive stresses, 0.5–5 nN/μm. This net force was then incorporated into a viscoelastic model of *Dictyostelium* mechanics [77].

$$\ddot{x} + \frac{k_c}{\gamma_c}\dot{x} = \left(\frac{1}{\gamma_c} + \frac{1}{\gamma_a}\right)\dot{\sigma}_x + \frac{k_c}{\gamma_c}\sigma_x$$

In this model, σ_x represents the x-component of the stress, with the viscoelastic parameters detailed in Table 4. A corresponding formula is used to denote displacement in the y-direction. The input to this linear viscoelastic model is derived from PKB activity, specifically $\sigma_x \propto [\mathrm{PKB}]$. The resultant displacements were normalized so that the maximum movement is equivalent to 10 μm/min.

Kymographs and heatmaps

For each model, the strengths of positive and negative feedback were varied from 0 to 20 in increments of 0.2. Each parameter set was simulated 20 times. PKB activity was visualized as kymographs, where the horizontal axis represents time and the vertical axis represents membrane activity. These kymographs were binarized, and activity patches were identified and analyzed using the `regionprops` function in MATLAB (MathWorks, Natick, MA). The following properties were measured: area, spatial extent, duration, and orientation. Patches were sorted in descending order based on area, and those smaller than 50 pixels were excluded from further analysis.

Heatmaps were generated to visualize the population-averaged trends in patch dynamics across parameter variations. The following metrics were analyzed:

1. **Mean patch width:** The kymographs were binarized to identify patches and MATLAB's `BoundingBox` command was used to determine the spatial and temporal boundaries of each patch. The spatial width was averaged across all patches within each simulation, and the mean values were plotted as a heatmap.
2. **Duration of the longest patch:** The temporal extent of each patch was extracted using `BoundingBox`. The duration of the largest patch (by area) within each simulation was recorded, and the average across simulations was visualized.
3. **Patch frequency:** To assess persistent activity patterns, transient patches were filtered out. At each time point, the number of patches present on the membrane was counted. The most frequently observed patch count over the simulation defined the kymograph's dominant state, which was then mapped across parameter space.

Table 4. Viscoelastic parameters [77].

Parameter	Value	Units
γ_a	6.09	nN s/μm^3
γ_c	0.064	nN s/μm3
k_c	0.98	nN/μm^3

https://doi.org/10.1371/journal.pcbi.1013036.t004

4. **Polarization duration:** A cell was considered polarized when exactly one membrane patch was present. The percentage of simulation time spent in this state was recorded and visualized as a heatmap.

Determination of polarized cells: A cell was classified as polarized if it met the following criteria:

- The most frequent number of membrane patches throughout the simulation was one.
- The cell spent more than 10% of the total simulation time in the polarized state.

To exclude hyperactive cells with a single, large patch covering most of the membrane, cells with a patch orientation angle exceeding 60° were excluded. The total number of simulations meeting these criteria was reported as the number of polarized cells.

Dictyostelium experiments

Dictyostelium cells were used to observe signaling activity (Fig 2) and quantify movement (Fig 3).

Cells and plasmids: *Dictyostelium discoideum* cells were cultured in HL5 media for a maximum of 2 months after thawing from frozen stock. AX3 cells were obtained from the R. Kay laboratory (MRC Laboratory of Molecular Biology, UK).

Plasmids were introduced into *Dictyostelium* cells using electroporation. To improve efficiency, heat-killed *Klebsiella aerogenes* was added after transformation. pDM358 RBD-EGFP, based on the 51–220 amino acids of Raf, was previously created in the Devreotes lab.

Microscopy: Cells were seeded in 8-well Lab-Tek chambers (Thermo-Fisher, 155409) and left to settle for ten minutes before the media was gently aspirated and replaced with Development Buffer (DB) (5 mM Na_2HPO_4, 5 mM KH_2PO_4, 1 mM $CaCl_2$, 2 mM $MgCl_2$). Cells were allowed to sit for an hour starving in DB prior to imaging to decrease photosensitivity. For experiments with polarized cells, growth-phase cells were washed and suspended in DB at a density of 2×10^7 cells/ml. Cells were then developed by being shaken for 1 hour and subsequently pulsed with 50–100 nM cAMP every 6 minutes and shaken for 4 hours.

Laser scanning confocal imaging was carried out on two microscopes: a Zeiss AxioObserver inverted microscope with an LSM800 confocal module and a Zeiss AxioObserver with 880-Quasar confocal module and Airyscan FAST module. On the LSM800 microscope, GFP and YFP proteins were excited with a solid-state 488 nm laser and on the 880 with an argon laser. Emission wavelengths collected were chosen to avoid overlap between GFP and mCherry emission profiles. All imaging was done with 63×/1.4 PlanApo oil DIC objectives and appropriate raster zoom. Brightfield images were acquired using a transmitted-photomultiplier tube (T-PMT) detector.

Spinning disk confocal imaging was performed on a Nikon TiE2 CSU W1 SoRA microscope, a solid-state 488 nm laser, a 60×/1.49 Apo TIRF objective, and a Hamamatsu FusionBT camera. Camera binning was adjusted to optimize for signal-to-noise ratio, resolution, and speed of acquisition. All images for a given experiment were acquired at the same binning.

Preparation of reagents and inhibitors: For experiments with Latrunculin (Fig 2), 2.5 μl aliquots of 1 mM Latrunculin in DMSO (Millipore Sigma, 428026) were diluted 1:20 in DB to make a 10× (50 μM) stock. 50 μl of this stock was then added to a well containing 450 μl of media prior to imaging. Cells were incubated in Latrunculin for at least 10 minutes prior to the start of the experiment.

KikGR optogenetic florescence to study dynamic partitioning of PIP5K: PIP5K (phosphatidylinositol 4-phosphate 5-kinase) photoconversion can be achieved using KiKGR, a green-to-red photoconvertible fluorescent protein. KiKGR is initially fluorescent green when excited with 488 nm light. Upon exposure to blue and near-ultraviolet light (405nm), it undergoes an irreversible photoconversion, shifting its emission from green (516 nm) to red (593 nm). This property is used to mark specific regions or populations of proteins in living cells and then track their movement over time.

PIP5K is genetically fused to KiKGR, allowing the fluorescent tag to report on the localization and dynamics of the kinase. Before photoconversion, the fusion protein fluoresces green, highlighting the regions where PIP5K is localized (often at the plasma membrane or specific intracellular compartments). A targeted area of the cell is exposed to 405 nm light using a laser-scanning confocal microscope. This exposure converts KiKGR from green to red in the illuminated region, without affecting unexposed areas. After photoconversion: The red fluorescence represents the PIP5K molecules present at the moment of photoconversion. The green fluorescence represents newly synthesized or newly trafficked PIP5K molecules.

By imaging both channels over time, you can track: PIP5K turnover rates from how fast the green signal fades as new red protein appears; protein trafficking from movement of red-labeled PIP5K from one cellular region to another; and diffusion dynamics, if the photoconverted region spreads over time.

Cell tracking and classification: Cell tracking in Fig 3 was performed using the TrackMate plugin in ImageJ. The plugin employs an intensity thresholding approach to distinguish the foreground from the background and connects regions with similar intensities within enclosed boundaries. For each identified region, several properties were measured, including mean intensity, orientation, circularity, and the position of the centroid. To track the trajectories of individual cells over time, the Linear Assignment Problem (LAP) tracker was utilized, allowing for accurate linking of detected spots across sequential frames. The mean circularity values obtained from the segmentation process were further used to classify cells into unpolarized, polarized, and intermediate polarized states. This classification was based on a negative correlation observed between cell speed and circularity, determined by linear regression analysis.

Kymograph generation for membrane activity of live cells: Kymographs representing membrane activity along the cell perimeter over time were generated from binarized image stacks of individual cells. Inner and outer radii were defined relative to the cell centroid using the bounding box properties from the `regionprops` function in MATLAB, ensuring coverage of the entire cell boundary. Membrane intensity (IM) at equally spaced points along the perimeter was quantified by performing 1-pixel-wide linescans perpendicular to the boundary. The length of each linescan was adjusted based on the defined inner and outer radii to ensure complete coverage of the boundary across all angles. For each linescan, IM was calculated as the average of the three brightest pixels. These intensity values were plotted as a function of time and perimeter angle to construct the kymograph.

HL-60 experiments

Neutrophil-like HL60 cells were used to observe the effect of various pharmacological interventions on cell activity (Fig 7).

Reagents and inhibitors: 200 μg/ml fibronectin stock (Sigma-Aldrich; Cat #F4759-2MG) was prepared in sterile water, and subsequently diluted in 1x PBS. 10 μM Latrunculin B (Sigma-Aldrich; Cat #428020) or 50 mM CK666 (EMD Millipore; Cat #182515) stock was prepared in dimethyl sulfoxide (DMSO, Sigma-Aldrich; Cat #D2650). Phorbol 12-myristate

13-acetate (PMA, Sigma-Aldrich; Cat #P8139) was dissolved in DMSO to make 1 mM stock. Puromycin (Sigma-Aldrich; Cat #P8833) or blasticidin S (Sigma-Aldrich; Cat #15205) was prepared in sterile water to make stock solution of 2.5 mg/ml or 10 mg/ml, respectively. Aliquots of all stock solutions were stored at –20 °C. According to experimental requirements, further dilutions were prepared in 1 × PBS or culture medium before adding to cells.

Cell culture: Female human HL-60 cells were grown in RPMI 1640 medium (Gibco; Cat #22400-089) supplemented with 15% heat-inactivated fetal bovine serum (Thermo Fisher; Cat #16140071) as described previously [70,71]. To obtain migration-competent neutrophils or macrophages, WT or stable lines were differentiated in the presence of 1.3% DMSO over 6–8 days or 32 nM PMA for 2–3 days, respectively [56,70,71]. All cells were maintained in humidified conditions at 5% CO_2 and 37 °C. Stable cells were maintained in the presence of selection antibiotics, which were removed during differentiation and experimentation.

Plasmid construction and transfection: All DNA oligonucleotides were procured from Sigma-Aldrich. CRY2PHR–mCherry–KRas4B G12VΔCAAX/pPB (Addgene #201753), CIBN–CAAX/pLJM1 (Addgene #201749) or LifeAct–miRFP703/pLJM1 (Addgene #201750) construct was generated in a previous study [70,71]. DNA sequence (996 bases) encoding the 5-phosphatase, INP54P, was PCR-amplified and sub-cloned into the BspEI and SalI sites of the PiggyBac transposon plasmid to create CRY2PHR-mCherry-INP54P/pPB construct. All constructs were verified by diagnostic restriction digestion and sequenced at the institutional sequencing facility.

HL-60 cells stably co-expressing CIBN-CAAX, LifeAct-miRFP703, and opto-KRas4B G12VΔCAAX were constructed earlier [70,71]. Here, we introduced 5 μg opto-INP54P construct with an equal amount of PiggyBac transposase plasmid in the CIBN-CAAX and LifeAct-miRFP703 co-expressing HL-60 stable cell line using Neon transfection system 100 μl kit (Thermo Fisher; Cat #MPK10025). Cells were selected in the presence of puromycin and blasticidine S.

Confocal microscopy and optogenetics: Differentiated neutrophils or macrophages were adhered on an eight-well coverslip chamber in the presence or absence of fibronectin, respectively. Next, fresh RPMI 1640 medium was added to attached cells and used for imaging. All imaging was performed at a middle plane of the cells with 0.2–10% laser intensity using a Zeiss LSM780-FCS single-point, laser scanning confocal microscope supported with ZEN Black software. Images were acquired with a 40 × /1.30 PlanNeofluar oil DIC objective, in addition to digital zoom. For inhibitor experiments, cells were treated with 50 μM CK666 or 5 μM Latrunculin B for at least 10 minutes before imaging [56,70,71].

Optogenetic experiments were done in the absence of any chemoattractant, as described previously [56,70,71]. Briefly, a solid-state laser (561 nm excitation and 579–632 nm emission) was used for visualizing opto-KRas4B G12VΔCAAX or opto-INP54P whereas a diode laser (633 nm excitation and 659–709 nm emission) was utilized to capture LifeAct-miRFP703 expression. Images were acquired for approximately 5 minutes, after which a 450/488 nm excitation laser was turned on globally to activate INP54P or KRas4B G12VDCAAX recruitment. Image acquisition and photoactivation were done at 7-second intervals.

Supporting information

S1 Fig. Sample experimental kymographs of *Dictyostelium* cells with varying polarization levels. Kymographs showing the normalized membrane localization of RasGTP (RBD-GFP) in unpolarized (A), intermediate polarized (B), and fully polarized (C) cells. All kymographs share the same time scale on the x-axis and length scale on the y-axis.
(TIFF)

S2 Fig. Bifurcation diagrams for the models of Fig 4A and Fig 5B.) Each dot represents the Ras equilibrium value assuming no diffusion or noise as a function of the positive (a_{act}) and negative (a_{myo}/a_{ten}) feedback strengths. Both models show bistability, but that of global inhibition does so only for a restricted number of negative feedback strengths. The inset in panel B shows bistability and the equilibrium for these values.
(TIFF)

S3 Fig. Ras kymographs for a model incorporating positive feedback and both local and global negative feedback. Feedback strengths of the various loops were varied as shown.
(EPS)

S4 Fig. Model used to determine PIP5K sensitivity. A. Schematic of a system in which varying levels of PIP5K alter the production rate of PIP2 in STEN (parameter b_1 in Eq 2). The level PIP5K was set so that the production rate matched the basal level. B. Sample kymograph for this system when PIP5K=1. C. Effect on the excitable system activation threshold when the production level was changed by varying PIP5K levels. Around PIP5K, the system is excitable and shows an increase in the threshold (the system is harder to trigger) as PIP5K increases. There is some biphasic behavior, with the threshold peaking around PIP5K≈ 4 (inset). Lowering PIP5K levels makes the system easier to trigger (lowering threshold) and eventually goes unstable at around PIP5K≈ 0.6, marked by the dotted line. Eventually, the system reaches a very high level of activity, denoted by the solid, gray line, at PIP5K≈ 0.5. The shaded region denotes the range of PIP5K levels that was observed in simulations; in this range, the threshold shows a monotonic dependence on PIP5K levels.
(TIFF)

S5 Fig. Global inhibition through reduction of RasGTP production. A. Schematic illustrating how positive and negative feedback influence the signaling pathway by modulating the degradation or production rate of Ras in different models. In the simulations of Fig 4 and Fig 5, the negative feedback is effected by increasing RasGTP hydrolysis of the RasGAP (Eq 6 and Eq 7, respectively.) In the simulations of this figure, the inhibition is achieved by reducing the guanine exchange by lowering the RasGEF action (Eq 8). All models used the same positive feedback which increases guanine exchange (Eq 5). B. Kymographs from simulations showing the effect of branched-actin-mediated positive feedback (ranging from 0 to 2 in steps of 0.2) and global negative feedback (ranging from 0 to 4.0 in steps of 0.4). C. Trajectories of simulated cells under varying feedback strengths, with 20 simulations per condition. Feedback strengths correspond to those in panel B. D. Heatmap showing the number of polarized cells in a population of 20 for each feedback strength condition represented in panels B and C.
(TIFF)

S6 Fig. Dynamic partitioning of PIP5K using KikGR. A. Representative live-cell time-lapse images of *Dictyostelium* cells expressing KikGR-PIP5K. The yellow boxes indicate where laser-induced photoconversion from green to red took place (see 2 and 4 min panels). Imaging of GFP channel (488 nm) shows regions before photoconversion, while the RFP channel (561 nm) shows photoconverted fluorophores. B. Kymographs of the two channels for the cell in panel A showing the green signal and red signals.
(EPS)

S1 Video. Polarized cells. Time-lapse confocal microscopy of polarized *Dictyostelium* cells expressing GFP-RBD. Video corresponds to Fig 3A and S1 FigA. Tracks were added using TrackMate in Image J.
(MP4)

S2 Video. Intermediate polarized cell. Time-lapse confocal microscopy of intermediately polarized *Dictyostelium* cell expressing GFP-RBD. Video corresponds to Fig 3B and S1 FigB. Track was added using TrackMate in Image J.
(MP4)

S3 Video. Unpolarized cell. Time-lapse confocal microscopy of unpolarized *Dictyostelium* cell expressing GFP-RBD. Video corresponds to Fig 3C and S1 FigC. Track was added using TrackMate in Image J.
(MP4)

S4 Video. Ras activation in HL-60 neutrophil-like cells. Time-lapse confocal microscopy of differentiated HL-60 neutrophil-like cells expressing CRY2PHR-mCherry-KRas4B G12VΔCAAX(red; left) and LifeAct-miRFP703 (cyan; right) before and after laser illumination. The video corresponds to Fig 7A.
(MP4)

S5 Video. InP54p activation in HL-60 neutrophil-like cells. Time-lapse confocal microscopy of differentiated HL-60 neutrophil-like cells expressing CRY2PHR-mCherry-InP54p (red; left) and LifeAct-miRFP703 (cyan; right). The video corresponds to Fig 7B.
(MP4)

S6 Video. CK666 addition to neutrophil cells. Time-lapse confocal microscopy of differentiated HL-60 neutrophil-like cells expressing CRY2PHR-mCherry-KRas4B G12VΔCAAX (red; left) and LifeAct-miRFP703 (cyan; right) before and after the addition of CK666. The video corresponds to Fig 7C.
(MP4)

S7 Video. Latrunculin-treatment of neutrophil cells. Time-lapse confocal microscopy of differentiated HL-60 neutrophil-like cells expressing CRY2PHR-mCherry-KRas4B G12VΔCAAX (red; left) and LifeAct-miRFP703 (cyan; right) before and after the addition of Latrunculin B. The video corresponds to Fig 7D.
(MP4)

S8 Video. Dynamic partitioning. *Dictyostelium* cells expressing photoactivatable KikGR-PIP5K. The yellow box indicates the location where the photoconversion takes place. The GFP and RFP channels (488 nm and 561 nm) show KikGR before and after photoconversion, respectively. The video corresponds to S6 Fig.
(MP4)

Acknowledgments

We thank members of the Iglesias and Devreotes labs for useful discussions. Special thanks to Bedri Abubaker-Sharif for valuable insights on the computational models and Yiyan Lin for sharing her experimental results. Additional acknowledgment to Doug Robinson (JHU School of Medicine) for his feedback and insight.

Author contributions

Conceptualization: Parijat Banerjee, Peter N. Devreotes, Pablo A. Iglesias.

Data curation: Parijat Banerjee, Jonathan A. Kuhn, Dhiman Sankar Pal, Yu Deng, Tatsat Banerjee.

Formal analysis: Parijat Banerjee, Pablo A. Iglesias.

Funding acquisition: Peter N. Devreotes, Pablo A. Iglesias.

Investigation: Parijat Banerjee, Jonathan A. Kuhn, Dhiman Sankar Pal, Yu Deng, Tatsat Banerjee, Pablo A. Iglesias.

Methodology: Pablo A. Iglesias.

Project administration: Pablo A. Iglesias.

Resources: Peter N. Devreotes, Pablo A. Iglesias.

Software: Parijat Banerjee, Pablo A. Iglesias.

Supervision: Peter N. Devreotes, Pablo A. Iglesias.

Validation: Parijat Banerjee, Pablo A. Iglesias.

Visualization: Parijat Banerjee, Pablo A. Iglesias.

Writing – original draft: Parijat Banerjee, Pablo A. Iglesias.

Writing – review & editing: Jonathan A. Kuhn, Dhiman Sankar Pal, Yu Deng, Tatsat Banerjee, Peter N. Devreotes.

References

1. Parent CA, Blacklock BJ, Froehlich WM, Murphy DB, Devreotes PN. G protein signaling events are activated at the leading edge of chemotactic cells. Cell. 1998;95(1):81–91. https://doi.org/10.1016/s0092-8674(00)81784-5 PMID: 9778249
2. Janetopoulos C, Ma L, Devreotes PN, Iglesias PA. Chemoattractant-induced phosphatidylinositol 3,4,5-trisphosphate accumulation is spatially amplified and adapts, independent of the actin cytoskeleton. Proc Natl Acad Sci USA. 2004;101(24):8951–6. https://doi.org/10.1073/pnas.0402152101
3. Devreotes P, Janetopoulos C. Eukaryotic chemotaxis: distinctions between directional sensing and polarization. J Biol Chem. 2003;278(23):20445–8. https://doi.org/10.1074/jbc.R300010200 PMID: 12672811
4. Huang C-H, Tang M, Shi C, Iglesias PA, Devreotes PN. An excitable signal integrator couples to an idling cytoskeletal oscillator to drive cell migration. Nat Cell Biol. 2013;15(11):1307–16. https://doi.org/10.1038/ncb2859 PMID: 24142103
5. Hannezo E, Heisenberg C-P. Mechanochemical feedback loops in development and disease. Cell. 2019;178(1):12–25. https://doi.org/10.1016/j.cell.2019.05.052 PMID: 31251912
6. Weiner OD, Neilsen PO, Prestwich GD, Kirschner MW, Cantley LC, Bourne HR. A PtdInsP(3)- and Rho GTPase-mediated positive feedback loop regulates neutrophil polarity. Nat Cell Biol. 2002;4(7):509–13. https://doi.org/10.1038/ncb811 PMID: 12080346
7. Wang F, Herzmark P, Weiner OD, Srinivasan S, Servant G, Bourne HR. Lipid products of PI(3)Ks maintain persistent cell polarity and directed motility in neutrophils. Nat Cell Biol. 2002;4(7):513–8. https://doi.org/10.1038/ncb810 PMID: 12080345
8. Srinivasan S, Wang F, Glavas S, Ott A, Hofmann F, Aktories K, et al. Rac and Cdc42 play distinct roles in regulating PI(3,4,5)P3 and polarity during neutrophil chemotaxis. J Cell Biol. 2003;160(3):375–85. https://doi.org/10.1083/jcb.200208179 PMID: 12551955
9. Sasaki AT, Chun C, Takeda K, Firtel RA. Localized Ras signaling at the leading edge regulates PI3K, cell polarity, and directional cell movement. J Cell Biol. 2004;167(3):505–18. https://doi.org/10.1083/jcb.200406177 PMID: 15534002
10. Sun CX, Downey GP, Zhu F, Koh ALY, Thang H, Glogauer M. Rac1 is the small GTPase responsible for regulating the neutrophil chemotaxis compass. Blood. 2004;104(12):3758–65. https://doi.org/10.1182/blood-2004-03-0781 PMID: 15308574
11. Weiner OD, Rentel MC, Ott A, Brown GE, Jedrychowski M, Yaffe MB, et al. Hem-1 complexes are essential for Rac activation, actin polymerization, and myosin regulation during neutrophil chemotaxis. PLoS Biol. 2006;4(2):e38. https://doi.org/10.1371/journal.pbio.0040038 PMID: 16417406
12. Charest PG, Firtel RA. Big roles for small GTPases in the control of directed cell movement. Biochem J. 2007;401(2):377–90. https://doi.org/10.1042/BJ20061432 PMID: 17173542

13. Sasaki AT, Janetopoulos C, Lee S, Charest PG, Takeda K, Sundheimer LW, et al. G protein-independent Ras/PI3K/F-actin circuit regulates basic cell motility. J Cell Biol. 2007;178(2):185–91. https://doi.org/10.1083/jcb.200611138 PMID: 17635933
14. Inoue T, Meyer T. Synthetic activation of endogenous PI3K and Rac identifies an AND-gate switch for cell polarization and migration. PLoS One. 2008;3(8):e3068. https://doi.org/10.1371/journal.pone.0003068 PMID: 18728784
15. Yoo SK, Deng Q, Cavnar PJ, Wu YI, Hahn KM, Huttenlocher A. Differential regulation of protrusion and polarity by PI3K during neutrophil motility in live zebrafish. Dev Cell. 2010;18(2):226–36. https://doi.org/10.1016/j.devcel.2009.11.015 PMID: 20159593
16. Miao Y, Bhattacharya S, Banerjee T, Abubaker-Sharif B, Long Y, Inoue T, et al. Wave patterns organize cellular protrusions and control cortical dynamics. Mol Syst Biol. 2019;15(3):e8585. https://doi.org/10.15252/msb.20188585 PMID: 30858181
17. Banerjee T, Biswas D, Pal DS, Miao Y, Iglesias PA, Devreotes PN. Spatiotemporal dynamics of membrane surface charge regulates cell polarity and migration. Nat Cell Biol. 2022;24(10):1499–515. https://doi.org/10.1038/s41556-022-00997-7 PMID: 36202973
18. Dalous J, Burghardt E, Müller-Taubenberger A, Bruckert F, Gerisch G, Bretschneider T. Reversal of cell polarity and actin-myosin cytoskeleton reorganization under mechanical and chemical stimulation. Biophys J. 2008;94(3):1063–74. https://doi.org/10.1529/biophysj.107.114702 PMID: 17905847
19. Lee S, Shen Z, Robinson DN, Briggs S, Firtel RA. Involvement of the cytoskeleton in controlling leading-edge function during chemotaxis. Mol Biol Cell. 2010;21(11):1810–24. https://doi.org/10.1091/mbc.e10-01-0009 PMID: 20375144
20. Hadjitheodorou A, Bell GRR, Ellett F, Shastry S, Irimia D, Collins SR, et al. Directional reorientation of migrating neutrophils is limited by suppression of receptor input signaling at the cell rear through myosin II activity. Nat Commun. 2021;12(1):6619. https://doi.org/10.1038/s41467-021-26622-z PMID: 34785640
21. Jeon TJ, Lee D-J, Lee S, Weeks G, Firtel RA. Regulation of Rap1 activity by RapGAP1 controls cell adhesion at the front of chemotaxing cells. J Cell Biol. 2007;179(5):833–43. https://doi.org/10.1083/jcb.200705068 PMID: 18039932
22. Jeon TJ, Lee D-J, Merlot S, Weeks G, Firtel RA. Rap1 controls cell adhesion and cell motility through the regulation of myosin II. J Cell Biol. 2007;176(7):1021–33. https://doi.org/10.1083/jcb.200607072 PMID: 17371831
23. Mondal S, Bakthavatsalam D, Steimle P, Gassen B, Rivero F, Noegel AA. Linking Ras to myosin function: RasGEF Q, a Dictyostelium exchange factor for RasB, affects myosin II functions. J Cell Biol. 2008;181(5):747–60. https://doi.org/10.1083/jcb.200710111 PMID: 18504297
24. Kuhn J, Banerjee P, Haye A, Robinson DN, Iglesias PA, Devreotes PN. Complementary cytoskeletal feedback loops control signal transduction excitability and cell polarity. Nat Commun. 2025;16(1):7482. https://doi.org/10.1038/s41467-025-62799-3 PMID: 40796751
25. Turing AM. The chemical basis of morphogenesis. Philos Trans R Soc Lond B Biol Sci. 1952;237(641):37–72.https://doi.org/10.1098/rstb.1952.0012
26. Gierer A, Meinhardt H. A theory of biological pattern formation. Kybernetik. 1972;12(1):30–9. https://doi.org/10.1007/BF00289234 PMID: 4663624
27. Fitzhugh R. Impulses and Physiological States in Theoretical Models of Nerve Membrane. Biophys J. 1961;1(6):445–66. https://doi.org/10.1016/s0006-3495(61)86902-6 PMID: 19431309
28. Nagumo J, Arimoto S, Yoshizawa S. An active pulse transmission line simulating nerve axon. Proc IRE. 1962;50(10):2061–70. https://doi.org/10.1109/jrproc.1962.288235
29. Weiner OD, Marganski WA, Wu LF, Altschuler SJ, Kirschner MW. An actin-based wave generator organizes cell motility. PLoS Biol. 2007;5(9):e221. https://doi.org/10.1371/journal.pbio.0050221 PMID: 17696648
30. Whitelam S, Bretschneider T, Burroughs NJ. Transformation from spots to waves in a model of actin pattern formation. Phys Rev Lett. 2009;102(19):198103. https://doi.org/10.1103/PhysRevLett.102.198103 PMID: 19519000
31. Ryan GL, Petroccia HM, Watanabe N, Vavylonis D. Excitable actin dynamics in lamellipodial protrusion and retraction. Biophysical Journal. 2012;102(7):1493–502. https://doi.org/10.1016/j.bpj.2012.03.005
32. Hecht I, Kessler DA, Levine H. Transient localized patterns in noise-driven reaction-diffusion systems. Phys Rev Lett. 2010;104(15):158301. https://doi.org/10.1103/PhysRevLett.104.158301 PMID: 20482022
33. Xiong Y, Huang C-H, Iglesias PA, Devreotes PN. Cells navigate with a local-excitation, global-inhibition-biased excitable network. Proc Natl Acad Sci U S A. 2010;107(40):17079–86. https://doi.org/10.1073/pnas.1011271107 PMID: 20864631

34. Taniguchi D, Ishihara S, Oonuki T, Honda-Kitahara M, Kaneko K, Sawai S. Phase geometries of two-dimensional excitable waves govern self-organized morphodynamics of amoeboid cells. Proc Natl Acad Sci U S A. 2013;110(13):5016–21. https://doi.org/10.1073/pnas.1218025110 PMID: 23479620
35. Nishikawa M, Hörning M, Ueda M, Shibata T. Excitable signal transduction induces both spontaneous and directional cell asymmetries in the phosphatidylinositol lipid signaling system for eukaryotic chemotaxis. Biophys J. 2014;106(3):723–34. https://doi.org/10.1016/j.bpj.2013.12.023 PMID: 24507613
36. Wang X, Carlsson AE. Feedback mechanisms in a mechanical model of cell polarization. Phys Biol. 2014;11(6):066002. https://doi.org/10.1088/1478-3975/11/6/066002 PMID: 25313164
37. Fukushima S, Matsuoka S, Ueda M. Excitable dynamics of Ras triggers spontaneous symmetry breaking of PIP3 signaling in motile cells. J Cell Sci. 2019;132(5):jcs224121. https://doi.org/10.1242/jcs.224121 PMID: 30745337
38. Shi C, Huang C-H, Devreotes PN, Iglesias PA. Interaction of motility, directional sensing, and polarity modules recreates the behaviors of chemotaxing cells. PLoS Comput Biol. 2013;9(7):e1003122. https://doi.org/10.1371/journal.pcbi.1003122 PMID: 23861660
39. Bement WM, Leda M, Moe AM, Kita AM, Larson ME, Golding AE, et al. Activator-inhibitor coupling between Rho signalling and actin assembly makes the cell cortex an excitable medium. Nat Cell Biol. 2015;17(11):1471–83. https://doi.org/10.1038/ncb3251 PMID: 26479320
40. van Haastert PJM, Keizer-Gunnink I, Kortholt A. Coupled excitable Ras and F-actin activation mediates spontaneous pseudopod formation and directed cell movement. Mol Biol Cell. 2017;28(7):922–34. https://doi.org/10.1091/mbc.E16-10-0733 PMID: 28148648
41. Tanabe Y, Kamimura Y, Ueda M. Parallel signaling pathways regulate excitable dynamics differently to mediate pseudopod formation during eukaryotic chemotaxis. J Cell Sci. 2018;131(23):jcs214775. https://doi.org/10.1242/jcs.214775 PMID: 30404836
42. Shao D, Rappel W-J, Levine H. Computational model for cell morphodynamics. Phys Rev Lett. 2010;105(10):108104. https://doi.org/10.1103/PhysRevLett.105.108104 PMID: 20867552
43. Shao D, Levine H, Rappel W-J. Coupling actin flow, adhesion, and morphology in a computational cell motility model. Proc Natl Acad Sci U S A. 2012;109(18):6851–6. https://doi.org/10.1073/pnas.1203252109 PMID: 22493219
44. Campbell EJ, Bagchi P. A computational model of amoeboid cell motility in the presence of obstacles. Soft Matter. 2018;14(28):5741–63. https://doi.org/10.1039/c8sm00457a PMID: 29873659
45. Neilson MP, Veltman DM, van Haastert PJM, Webb SD, Mackenzie JA, Insall RH. Chemotaxis: a feedback-based computational model robustly predicts multiple aspects of real cell behaviour. PLoS Biol. 2011;9(5):e1000618. https://doi.org/10.1371/journal.pbio.1000618 PMID: 21610858
46. Alonso S, Stange M, Beta C. Modeling random crawling, membrane deformation and intracellular polarity of motile amoeboid cells. PLoS ONE. 2018;13(8):e0201977. https://doi.org/10.1371/journal.pone.0201977
47. Camley BA, Zhao Y, Li B, Levine H, Rappel W-J. Crawling and turning in a minimal reaction-diffusion cell motility model: coupling cell shape and biochemistry. Phys Rev E. 2017;95(1–1):012401. https://doi.org/10.1103/PhysRevE.95.012401 PMID: 28208438
48. Moure A, Gomez H. Influence of myosin activity and mechanical impact on keratocyte polarization. Soft Matter. 2020;16(22):5177–94. https://doi.org/10.1039/d0sm00473a PMID: 32459252
49. Tao K, Wang J, Kuang X, Wang W, Liu F, Zhang L. Tuning cell motility via cell tension with a mechanochemical cell migration model. Biophys J. 2020;118(12):2894–904. https://doi.org/10.1016/j.bpj.2020.04.030 PMID: 32416081
50. Cao Y, Ghabache E, Miao Y, Niman C, Hakozaki H, Reck-Peterson SL, et al. A minimal computational model for three-dimensional cell migration. J R Soc Interface. 2019;16(161):20190619. https://doi.org/10.1098/rsif.2019.0619 PMID: 31847757
51. Marée AFM, Grieneisen VA, Edelstein-Keshet L. How cells integrate complex stimuli: the effect of feedback from phosphoinositides and cell shape on cell polarization and motility. PLoS Comput Biol. 2012;8(3):e1002402. https://doi.org/10.1371/journal.pcbi.1002402 PMID: 22396633
52. Stinner B, Bretschneider T. Mathematical modelling in cell migration: tackling biochemistry in changing geometries. Biochem Soc Trans. 2020;48(2):419–28. https://doi.org/10.1042/BST20190311 PMID: 32239187
53. Kabacoff C, Xiong Y, Musib R, Reichl EM, Kim J, Iglesias PA, et al. Dynacortin facilitates polarization of chemotaxing cells. BMC Biol. 2007;5:53. https://doi.org/10.1186/1741-7007-5-53 PMID: 18039371

54. Houk AR, Jilkine A, Mejean CO, Boltyanskiy R, Dufresne ER, Angenent SB, et al. Membrane tension maintains cell polarity by confining signals to the leading edge during neutrophil migration. Cell. 2012;148(1–2):175–88. https://doi.org/10.1016/j.cell.2011.10.050 PMID: 22265410
55. De Belly H, Yan S, Borja da Rocha H, Ichbiah S, Town JP, Zager PJ, et al. Cell protrusions and contractions generate long-range membrane tension propagation. Cell. 2023;186(14):3049-3061.e15. https://doi.org/10.1016/j.cell.2023.05.014 PMID: 37311454
56. Lin Y, Pal DS, Banerjee P, Banerjee T, Qin G, Deng Y, et al. Ras suppression potentiates rear actomyosin contractility-driven cell polarization and migration. Nat Cell Biol. 2024;26(7):1062–76. https://doi.org/10.1038/s41556-024-01453-4 PMID: 38951708
57. Li X, Edwards M, Swaney KF, Singh N, Bhattacharya S, Borleis J, et al. Mutually inhibitory Ras-PI(3,4)P 2 feedback loops mediate cell migration. Proc Natl Acad Sci USA. 2018;115(39). https://doi.org/10.1073/pnas.1809039115
58. Banerjee T, Deng Y, Pal DS, Zhan H, Iglesias PA, Devreotes PN. Signaling and actin waves at a glance. J Cell Sci. 2025;138(16):jcs263634. https://doi.org/10.1242/jcs.263634 PMID: 40843611
59. Deng Y, Banerjee T, Pal DS, Banerjee P, Zhan H, Borleis J, et al. PIP5K-Ras bistability initiates plasma membrane symmetry breaking to regulate cell polarity and migration. bioRxiv. 2024;:2024.09.15.613115. https://doi.org/10.1101/2024.09.15.613115 PMID: 39314378
60. Subramanian KK, Narang A. A mechanistic model for eukaryotic gradient sensing: spontaneous and induced phosphoinositide polarization. J Theor Biol. 2004;231(1):49–67. https://doi.org/10.1016/j.jtbi.2004.05.024 PMID: 15363929
61. Otsuji M, Ishihara S, Co C, Kaibuchi K, Mochizuki A, Kuroda S. A mass conserved reaction-diffusion system captures properties of cell polarity. PLoS Comput Biol. 2007;3(6):e108. https://doi.org/10.1371/journal.pcbi.0030108 PMID: 17559299
62. Iglesias PA, Devreotes PN. Navigating through models of chemotaxis. Curr Opin Cell Biol. 2008;20(1):35–40. https://doi.org/10.1016/j.ceb.2007.11.011 PMID: 18207721
63. Mori Y, Jilkine A, Edelstein-Keshet L. Wave-pinning and cell polarity from a bistable reaction-diffusion system. Biophys J. 2008;94(9):3684–97. https://doi.org/10.1529/biophysj.107.120824 PMID: 18212014
64. Jilkine A, Edelstein-Keshet L. A comparison of mathematical models for polarization of single eukaryotic cells in response to guided cues. PLoS Comput Biol. 2011;7(4):e1001121. https://doi.org/10.1371/journal.pcbi.1001121 PMID: 21552548
65. Ku C-J, Wang Y, Weiner OD, Altschuler SJ, Wu LF. Network crosstalk dynamically changes during neutrophil polarization. Cell. 2012;149(5):1073–83. https://doi.org/10.1016/j.cell.2012.03.044 PMID: 22632971
66. Rappel W-J, Edelstein-Keshet L. Mechanisms of cell polarization. Current Opinion in Systems Biology. 2017;3:43–53. https://doi.org/10.1016/j.coisb.2017.03.005
67. Meinhardt H. Orientation of chemotactic cells and growth cones: models and mechanisms. J Cell Sci. 1999;112(Pt 17):2867–74. https://doi.org/10.1242/jcs.112.17.2867 PMID: 10444381
68. Banerjee T, Matsuoka S, Biswas D, Miao Y, Pal DS, Kamimura Y, et al. A dynamic partitioning mechanism polarizes membrane protein distribution. Nat Commun. 2023;14(1):7909. https://doi.org/10.1038/s41467-023-43615-2 PMID: 38036511
69. Tang M, Wang M, Shi C, Iglesias PA, Devreotes PN, Huang C-H. Evolutionarily conserved coupling of adaptive and excitable networks mediates eukaryotic chemotaxis. Nat Commun. 2014;5:5175. https://doi.org/10.1038/ncomms6175 PMID: 25346418
70. Pal DS, Lin Y, Zhan H, Banerjee T, Kuhn J, Providence S, et al. Optogenetic modulation of guanine nucleotide exchange factors of Ras superfamily proteins directly controls cell shape and movement. Front Cell Dev Biol. 2023;11:1195806. https://doi.org/10.3389/fcell.2023.1195806 PMID: 37492221
71. Pal DS, Banerjee T, Lin Y, de Trogoff F, Borleis J, Iglesias PA, et al. Actuation of single downstream nodes in growth factor network steers immune cell migration. Dev Cell. 2023;58(13):1170-1188.e7. https://doi.org/10.1016/j.devcel.2023.04.019 PMID: 37220748
72. Zhan H, Bhattacharya S, Cai H, Iglesias PA, Huang C-H, Devreotes PN. An excitable Ras/PI3K/ERK signaling network controls migration and oncogenic transformation in epithelial cells. Dev Cell. 2020;54(5):608-623.e5. https://doi.org/10.1016/j.devcel.2020.08.001 PMID: 32877650
73. Charest PG, Shen Z, Lakoduk A, Sasaki AT, Briggs SP, Firtel RA. A Ras signaling complex controls the RasC-TORC2 pathway and directed cell migration. Dev Cell. 2010;18(5):737–49. https://doi.org/10.1016/j.devcel.2010.03.017 PMID: 20493808
74. Gillespie DT. The chemical Langevin equation. J Chem Phys. 2000;113(1):297–306.

75. Arai Y, Shibata T, Matsuoka S, Sato MJ, Yanagida T, Ueda M. Self-organization of the phosphatidylinositol lipids signaling system for random cell migration. Proc Natl Acad Sci U S A. 2010;107(27):12399–404. https://doi.org/10.1073/pnas.0908278107 PMID: 20562345

76. Biswas D, Bhattacharya S, Iglesias PA. Enhanced chemotaxis through spatially regulated absolute concentration robustness. Intl J Robust Nonlinear Control. 2022;33(9):4923–44. https://doi.org/10.1002/rnc.6049

77. Yang L, Effler JC, Kutscher BL, Sullivan SE, Robinson DN, Iglesias PA. Modeling cellular deformations using the level set formalism. BMC Syst Biol. 2008;2:68. https://doi.org/10.1186/1752-0509-2-68 PMID: 18652669